


## Topical Review

# Helium-ion-beam nanofabrication: extreme processes and applications

Shixuan He<sup>1,2</sup>, Rong Tian<sup>1</sup>, Wei Wu<sup>3</sup>, Wen-Di Li<sup>4</sup> and Deqiang Wang<sup>1</sup> 

<sup>1</sup> Chongqing Key Laboratory of Multi-scale Manufacturing Technology, Chongqing Institute of Green and Intelligent Technology, Chinese Academy of Sciences, Chongqing 400714, People's Republic of China

<sup>2</sup> College of Physics, Sichuan University, Chengdu, Sichuan 610065, People's Republic of China

<sup>3</sup> Department of Electrical Engineering, University of Southern California, Los Angeles, CA 90089, United States of America

<sup>4</sup> Department of Mechanical Engineering, The University of Hong Kong, Pokfulam, Hong Kong, People's Republic of China

E-mail: [dqwang@cigit.ac.cn](mailto:dqwang@cigit.ac.cn)

Received 10 May 2020, revised 24 June 2020

Accepted for publication 30 October 2020

Published 23 November 2020



## Abstract

Helium ion beam (HIB) technology plays an important role in the extreme fields of nanofabrication. This paper reviews the latest developments in HIB technology as well as its extreme processing capabilities and widespread applications in nanofabrication. HIB-based nanofabrication includes direct-write milling, ion beam-induced deposition, and direct-write lithography without resist assistance. HIB nanoscale applications have also been evaluated in the areas of integrated circuits, materials sciences, nano-optics, and biological sciences. This review covers four thematic applications of HIB: (1) helium ion microscopy imaging for biological samples and semiconductors; (2) HIB milling and swelling for 2D/3D nanopore fabrication; (3) HIB-induced deposition for nanopillars, nanowires, and 3D nanostructures; (4) additional HIB direct writing for resist, graphene, and plasmonic nanostructures. This paper concludes with a summary of potential future applications and areas of improvement for HIB extreme nanofabrication technology.

Keywords: helium ion beam, extreme nanofabrication, direct writing, nanostructures

## Abbreviations

HIB	Helium Ion Beam	GIS	Gas Injection System
HIM	Helium Ion Microscopy	3D	Three-Dimensional
HIL	Helium Ion Lithography	2D	Two-Dimensional
GFIS	Gas Field Ion Source	FIB	Focused Ion Beam
SE	Secondary Electron	MLCC	Multilayer Ceramic Capacitor
SEM	Scanning Electron Microscope	AFM	Atomic Force Microscope
		TEM	Transmission Electron Microscopy
		CNM	Carbon Nanomembranes
		MoS <sub>2</sub>	Molybdenum Disulfide
		h-BN	hexagonal Boron Nitride
		EDS	Energy Dispersive Spectroscopy
		CPW	Coplanar Waveguide
		WC	Tungsten Carbide
		EBL	Electron Beam Lithography
		HSQ	Hydrogen Silsesquioxane
		Pt	Platinum



Original content from this work may be used under the terms of the [Creative Commons Attribution 3.0 licence](https://creativecommons.org/licenses/by/3.0/). Any further distribution of this work must maintain attribution to the author(s) and the title of the work, journal citation and DOI.

Co	Cobalt
W	Tungsten
ppt	Point Probe Test
DRAM	Dynamic Random Access Memory
IBID	Ion-Beam-Induced Deposition
GQDs	Graphene Quantum Dots

## 1. Introduction

Due to high resolution and sensitivity, nanofabrication technology is widely used to pattern nanostructures into components, devices, or systems for integrated circuits, materials sciences, nano-optics, and bio-sciences applications. The focused positive ion beam with a sub-nanometer spot-size is developed by using the gas field ion source (GFIS), which equips a three-sided pyramidal tip consisting of only three atoms at the apex (called a trimer) [1]. With its advantage of a sub-nanometer spot-size, helium ion microscopy (HIM) is a promising method for high-resolution imaging with secondary electron (SE) emission by generating a focused helium ion beam (HIB) from a GFIS. Helium gas molecules are field ionized on a cryogenically cooled tungsten (W) tip with a trimer. One of the HIBs emitted from three atoms of the trimer is chosen for the high-resolution HIM imaging. Changing the gas pressure allows for controlled operation of the HIB current between fA and pA levels to meet the high-resolution requirements of various applications [2, 3]. HIM has significant advantages over a focused ion beam (FIB) with gallium source and scanning electron microscope (SEM), including high-resolution, high-sensitivity, high-SE yield, and long-depth of focus with several novel contrast mechanisms for imaging applications [4]. For example, HIM is used for failure analysis of semiconductor devices by using voltage contrast theory [5]. Since scanning HIB slows SE charge accumulation, HIM can successfully image poorly conducting samples, such as uncoated biological samples [6, 7]. Therefore, HIM can be used for high-sensitivity and high-contrast imaging in the fields of semiconductors, materials sciences, and biological sciences fields with less damage to target samples.

Except for high-resolution imaging, HIM can also perform extremely complex direct-write nanofabrication [8]. While equipped with a gas injection system (GIS), HIM can pattern special structures through HIB-assisted milling and HIB-induced deposition processes [9]. The small focal spot and sharp beam source with the development of GFIS, and the unique interaction of the high-energy helium ions with the target at and just below the surface, enables HIM to perform ultrahigh-resolution nanopore fabrication on thin films or bulk materials to meet the requirements of single molecular detection in bioscience [10–13]. HIB bombardment can easily produce sub-10 nm diameter nanopores on freestanding material film with high reproducibility [14]. Sub-5 nm diameter nanopores can be obtained using optimized HIB milling parameters on suspended monolayer graphene, which is valuable for single-base biomolecule analysis to achieve DNA/RNA sequencing functions [15]. Using HIB technology, amorphization is one of the most important parts of the

bulk material milling process. Amorphization during the HIB milling process and materials swelling pave the way towards the fabrication of nano-volcano structures for potential nano-optical and biological science applications [16].

The energy and momentum of HIB promote the chemical reactions of precursor gas molecules on the surface. Scanning the HIB during continuous decomposition precursor gas molecules can result in direct deposition of materials with programmed three-dimensional (3D) structures. The HIB induces material deposition to create wires for future circuit editing and 3D structures for nano-electronic device applications [17]. The HIB-assisted milling process also increases the material removal rate because the chemical reaction requires a smaller dose of ions between the precursor gas molecules and the target-specific materials [18]. The maximum 41% platinum (Pt) content nanopillar and 10 nm resolution multiple cobalt (Co) lines are deposited by HIB-induced deposition at a rate of  $0.6 \mu\text{m}^3/\text{nC}$  with precursor gases [19]. Another major HIB nanofabrication mode is the direct writing pattern which works with or without resist assistance. Compared with FIB direct writing technique using heavy gallium ions, HIB direct writing is used in high pattern-density nanolithography with high-resolution and sensitivity due to its sub-nanometer spot size. The proximity effect has a less significant impact on patterning because the forward scattering is weaker and the yielded SEs diffuse small laterally [20]. Sub-10 nm scale nanochannels and nanoribbons can be directly patterned on a graphene membrane using HIB direct writing techniques for functional nanoscale graphene devices. Due to its high-resolution, HIM can pattern 1.5 nm structures by correcting the proximity effect [21, 22]. Plasmonic nanostructures fabricated with HIB direct writing techniques are used for molecular spectroscopy, near-field or nanoscale imaging, quantum mechanical phenomena applications [23, 24].

This review examines the extreme processes and applications of HIB nanofabrication. We discuss the advantages of HIM, including its high-resolution and high-sensitivity for extreme nanostructures fabrications. We follow with a review of studies using HIM for biological samples and semiconductors and an introduction of HIM system with GFIS. Then, HIB-related nanofabrication technologies are presented, which includes milling and swelling, ion beam induced deposition, and additional HIB nanofabrication, such as direct writing techniques. The nanostructures fabricated by the above technologies and their properties will be used to verify the feasibility and resolution of HIB nanofabrication. Finally, this review concludes with a summary of the latest progress in HIB nanofabrication and potential future developments in extreme processes and applications.

## 2. HIM system with GFIS

The basic components of a focus HIM system consist of an ion source, a column, a sample chamber with a substrate stage, and a vacuum chamber with auxiliary equipment (figure 1). The extremely bright GFIS in the HIB system was developed to achieve a smaller, sub-nanometer probe size based on a

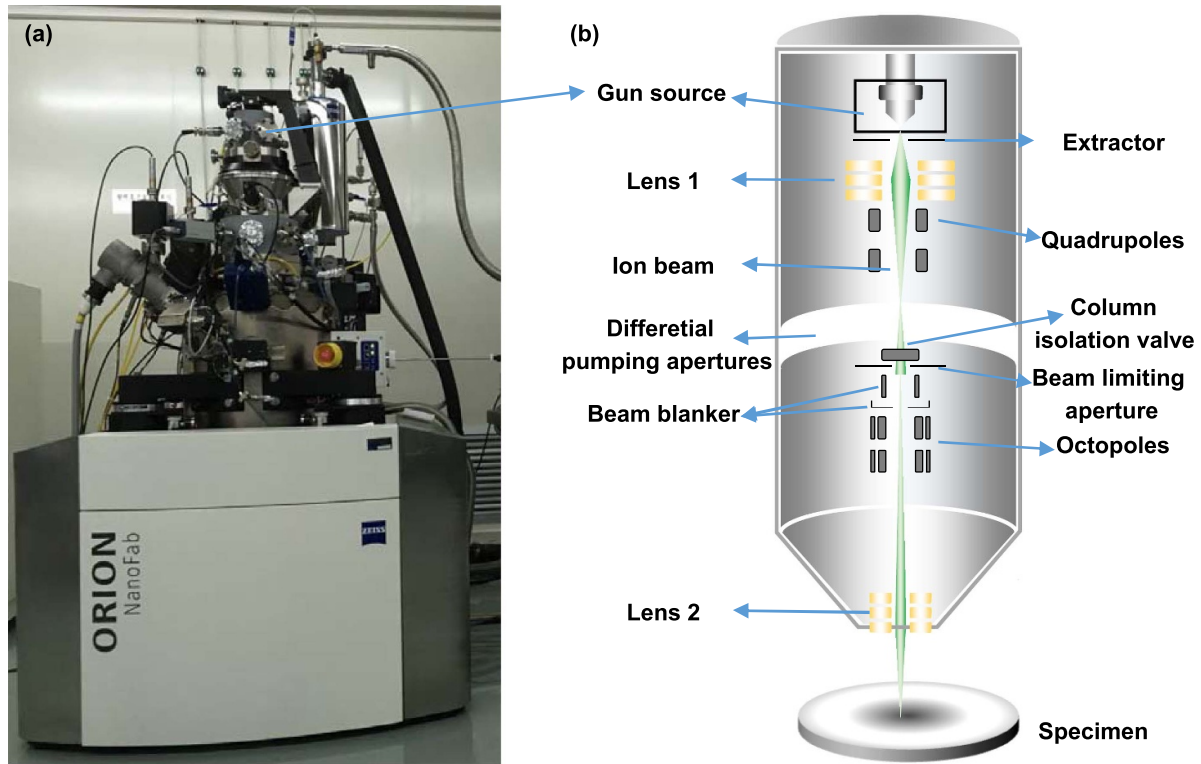


**Figure 1.** (a) HIM system (Orion NanoFab, Carl Zeiss) at CIGIT. (b) The schematic of the GFIS column.

needle-shaped W electrode called an ‘emitter’. Under a very larger electric field, high voltage is applied between the emitter and an adjacent grounded electrode. The emitter, with a sharp tip, prompts electrons from the helium atoms to escape because of the quantum-mechanical tunneling effect. The source produces positive ions by field ionization. These positive ions pass through the extractor plate. A continuous beam of helium ions is successfully obtained by accelerating these ions through the GFIS column. In the GFIS column, three atoms at the apex of the emitter, called a trimer, are used to ionize the helium gas, which forms the ion beam. A single beam is aligned to the optics column by carefully adjusting the lens 1, quadrupoles, octopoles, and lens 2. With the ultra-high brightness GFIS, the extremely narrow beam due to the atomic scale source, the use of helium ions, and the low energy spread makes HIM ideal as a high-resolution probe for imaging and nanofabrication [20].

### 3. HIM imaging

SEM is one of the basic techniques for imaging the exterior shape and structure of a sample [25]. Numerous advances in SEM imaging have been developed by controlling charge and maintaining the biological surface structure to increase topographical contrast and surface sensitivity [26]. However, SEM is limited in terms of resolution and contrast in the nanoscale applications. Recently, focused HIM has become an important microscopy technology for ultrahigh-resolution and high-contrast imaging [27, 28]. Since one atom at the apex is selected as the ion source for imaging, a very small  $\text{He}^+$  ion

beam spot size defines the aperture. Therefore, the HIM exhibits a higher resolution with a larger depth of field, neglecting the spherical and chromatic aberrations of the ion optical column [29, 30]. Since its development by Ward B W *et al* [31] in 2006, HIM has been applied in high-contrast imaging of conducting, semiconducting, and insulating materials, as well as biological samples [32].

#### 3.1. HIM imaging of biological samples

Bazou D *et al* demonstrated the possibility of HIM imaging for uncoated human colon cancer cells and its advantages in biological samples. Detailed morphological information, such as pores on the cell surface and overall cell surface roughness of uncoated human colon cancer cells, verifies the effectiveness of HIM imaging in biological samples, as shown in figure 2(a) [33]. As shown in figure 2(b), HIM can also acquire high-resolution images with 3D-like nanoscale fibril morphology details and fibril connections in samples without conductive coatings [34]. Based on its advantages of higher resolution and contrast, the HIM technique visualizes the surface ultrastructure of challenging biological samples without requiring metal coatings. Therefore, HIM preserves the subtle surface features that are typically obscured by metal coatings in SEM imaging. Figures 2(c) and (d) show that the low sputtering rate of HIM produces no discernable beam damage on the small and delicate surface features of biological samples [35–37]. HIM was used to imaging bacterial colonies and bacteria-phage interactions on a natural agar growth substrate at sub-nanometer resolution. For the first time, images depicting the

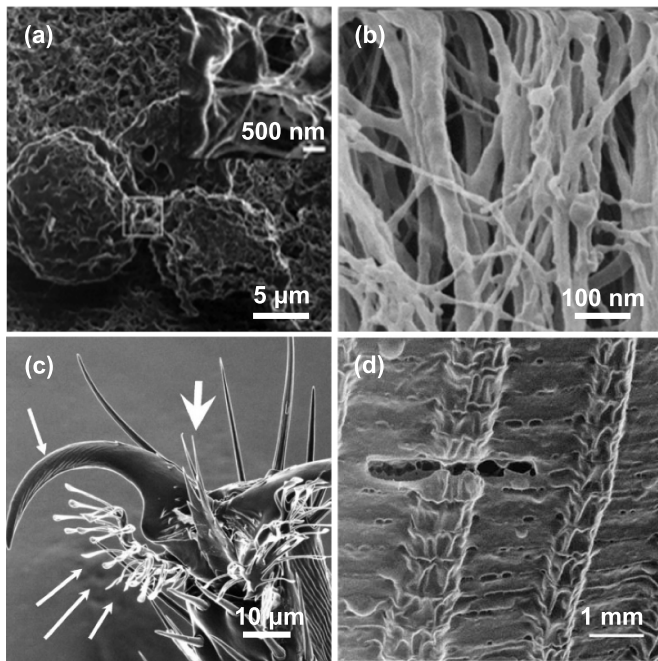


**Figure 2.** (a) HIM images of uncoated human colon cancer cell—Caco2 cells, an uncoated cell can shed light on such ambiguities—two separate cells are clearly shown. Reprinted with permission from [33]. Copyright 2011 John Wiley and Sons. (b) HIM image of microfibrillar mesh in the interior layer of collagen that surrounds cartilage cell. Reprinted with permission from [34]. Copyright 2012 John Wiley and Sons. (c) HIM image of drosophila melanogaster tarsus with the empodium (big arrowhead) that is flanked dorso-laterally by two tarsal claws (thick arrows) and ventrally by two sets of pulvilli (one pulvillus, group of thin arrows). Reprinted from [36] with permission from Elsevier. (d) HIM image of pristonchus pacificus, the delicate nature of the neon milling was demonstrated by the patterning of a small horizontal line using a dose of  $0.3 \text{ nC mm}^{-3}$ . Despite being strong enough to penetrate the outer cuticle of the nematode, minimal ablation and thermal damage are visible on the surrounding area [35].

different stages of a viral infection within host cells were obtained with HIM imaging technology [38]. HIM technology has also been used to show the detailed characteristics of conducting nanostructures on insulating cells. The above results highlight the potential of HIM technology to further understand the organic-inorganic interfaces of nanomaterials used in the biological field [39].

### 3.2. HIM imaging of semiconductors

Due to the high sensitivity of contrast attributes, HIM is widely used in semiconductors alongside voltage contrast imaging and doped contrast imaging [5]. The failure analysis of dynamic random access memory was developed with HIM by using the voltage contrast in semiconductor devices. The contrast between the silicon bulk and the oxide liners in the HIM image was more pronounced than in the SEM images, which was difficult to distinguish the continuous liner [29]. Furthermore, the voltage contrast in the HIM images of graphene nanoconductors fabricated by HIB maskless lithography was also used to test the electrical

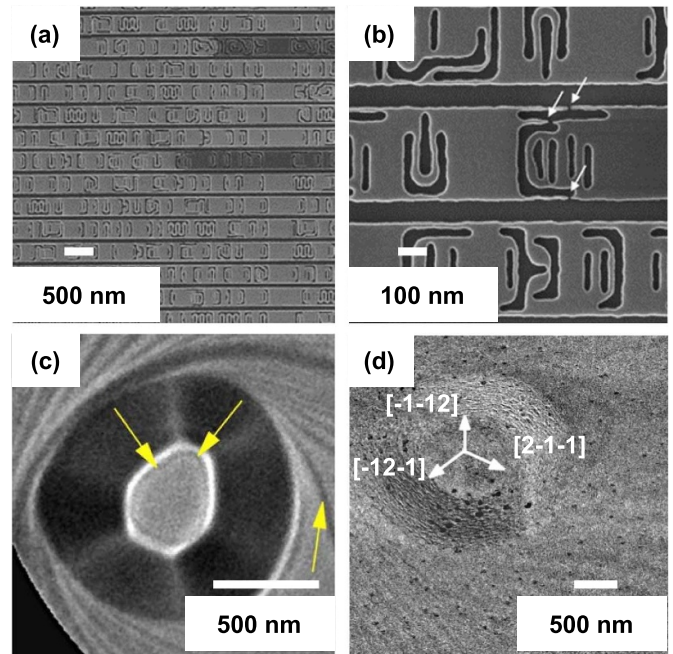


**Figure 3.** HIM image displaying voltage contrast over the defective region (a) and (b) enlarged view of one starting point of the defective stripe in the middle of the image from (a). Reprinted with permission from [43]. Copyright 2019 American Chemical Society. (c) Representative low energy electron microscopy image of a mound on the clean Pt (111) surface. The hexagonal shape of the mound is visible. A monatomic surface step on the top of the mound is marked with yellow arrows. (d) HIM image of a Pt mound on a single crystalline Pt (111) sample covered by 2–3 layers equivalent of Ag. White arrows indicate the threefold symmetry of the steps with 001 facet orientations. The labels give the projected surface directions in the (111) plane. Reprinted from [45] with permission from Elsevier.

conductivity characteristics of nanoelectronic devices *in situ* [40]. SE images of cross-sections of multilayer ceramic capacitors demonstrate that active voltage contrast can be used to investigate electrical potential differences between a ground electrode and a positively biased internal electrode [41]. HIM imaging technology can also map the nanometer-scale electrical potential distribution of Li-ion rechargeable batteries [42]. The defect localization for failure analysis of conductive structures, especially electronic devices, can be detected with passive voltage contrast in HIM images at the nanoscale, as shown in figures 3(a) and (b) [43]. It can detect defect gaps smaller than 10 nm. HIM imaging is an effective method for conducting structural failure analysis due to its higher resolution and ability to analyze a surface with minimal damage or implantation [44].

In the case of doped contrast imaging, Jepson M A E *et al* showed that HIM imaging can improve the lateral resolution in quantitative dopant mapping. For high doping levels, the contrast in HIM images is highly sensitive to changes in dopant concentration relative to SEM [46, 47]. With surface sensitivity and high lateral resolution, HIM can obtain information about the lattice structure of surface-confined alloys (figures 3(c) and (d)), including the single atomic layer steps

between terraces and the periodicities of the hcp/fcc pattern formed in a 2–3 layer thick alloy film [45]. Except for the acquisition of crystallographic information, HIM imaging can also be used to obtain information about ultrathin organic and inorganic layers, such as crystal defects and membrane thickness. Therefore, a new contrast mechanism for HIM imaging has been developed to suppress absorbed thin films from channeling into crystalline matter. It can visualize ultrathin layers of light elements on top of heavier substrates [48]. Using a custom scanning transmission ion microscopy stage, Hall A R [49] measured the local thickness of a freely suspended solid-state membrane thinned by a focused HIB. The relative brightness of the transmission image collected by the SE detector from the ions transmitted through the suspended membrane can be used to estimate the membrane thickness. To solve the challenge of measuring critical dimensions of complicated nanostructures, such as an atomic force microscope (AFM) tip characterizer, the scanning HIM can be used to characterize focal depth with SE images [50].

#### 4. HIB milling and swelling

In top-down micro- and nano-fabrications, the ion beam milling process involves bombarding the substrate surface with a beam of accelerated ions, which transfer their momentum to the target atoms. Then, the target atoms sputter out of the substrate in a controlled manner. The processing technology includes physical sputtering, material redeposition, and amorphization (e.g. swelling) processes. The development of GFIS technology can produce high brightness HIB. When HIB dwells on a target sample, the helium ions lose energy as they interact with the target material and sputter atoms during the milling process. Compared to gallium FIB milling,  $\text{He}^+$  ions have relatively low mass, which results in less damage to the sample. Therefore, the HIB milling process generates a lower milling yield but a more controlled fabrication process with a higher aspect ratio and higher accuracy. The focused HIB technology has distinct advantages in nanofabrication, including milling processes for local thickness control and nanostructure fabrication in free-standing membranes and bulk materials [51]. However, the amorphization and helium implantation during HIB milling may damage bulk substrates. Therefore, the optimization of ion dose, beam energy, and HIB dose rate is critical for local thickness manipulation and topography accuracy control in nanostructures fabrication [52].

##### 4.1. Milling for nanopore fabrications

In recent years, solid-state nanopore technology has become an important tool for detecting single biomolecules [10], especially in DNA/RNA sequencing applications [53]. The high-resolution requirements of solid-state nanopore technology prompted efforts to achieve precise control over nanopore size and membrane thickness. The characteristics of HIB milling technology, such as its small focal spot, sharp beam source, and the relatively low mass of  $\text{He}^+$ , make it is useful

for manipulating the local thickness of membranes and fabricating nanoscale pores.

Marshall M M *et al* [54] demonstrated that membrane thickness significantly effects the expansion rate of pores, which follows a reproducible trend in nanopore fabrication. The silicon nitride membranes were locally thinned to the appropriate thickness with HIM, and the nanopores were precisely fabricated in a fixed position by the controlled breakdown technique for single-molecule sensing applications [55, 56]. Marshall M M *et al* [54] also investigated aspects of direct and transmission HIB milling on suspended silicon nitride membranes for accurate thickness control. In addition to local thickness manipulation, topography accuracy control of nanostructures is another advantage of the HIB milling process. Xia D *et al* [14] used HIB milling technology to fabricate excellent, reproducible solid-state nanopores on the silicon nitride membranes over a large area (figure 4)(A). However, the bubble phenomenon often occurs during the HIB milling process of bulk materials. A volcano-like nanostructure, surrounded the milled region on the silicon nitride membranes and gradually decreased during nanopore fabrication [54].

Due to its highly focused GFIS and small beam-sample interaction volume, nanopore size is easily controlled when using a focused HIB with a diameter in the range of 10 nm or less, and as low as 1.3 nm in carbon nanomembranes (CNM), as shown in figure 4(B) [12]. Additionally, HIB milling technology can be used to rapidly fabricate nanopores on the two-dimensional (2D) membrane materials, such as molybdenum disulfide ( $\text{MoS}_2$ ) and hexagonal boron nitride (h-BN) for highly sensitive biomolecule analyses [58, 59]. The sub-10 nm nanopores in the h-BN lattice membrane passivated the dangling bonds of graphene quantum dots (GQDs). This made the GQDs highly stable while maintaining their intrinsic quantum properties [57] (figure 4)(C).

The thinness of 2D materials, such as graphene and  $\text{MoS}_2$ , promotes the use of HIM-based rapid fabrication processes in nanopore technology applications. The impact of helium ion bombardment on freestanding thin membranes is essential for nanoscale accuracy control and biomolecule detection applications. Therefore, Raman spectroscopy was used to analyze the amorphization and defects on HIB-damaged free-standing graphene and supported graphene [60, 61]. A large fraction of helium ions passed through the free-standing graphene membrane, causing minimal damage to its lattice state. However, helium ion collisions can destroy the lattice, forming vacancy defects in the freestanding 2D materials membranes. Therefore, optimizing HIB parameters is crucial for fabricating high-quality graphene nanopores, while minimizing the effect of amorphization on nanopore fabrication during HIB milling. HIB technology can produce high-quality, sub-5 nm graphene nanopores by precisely controlling the milling parameters (figure 5). The diameters of graphene nanopores expand at a faster rate during short periods of HIB bombardment whereas longer exposure times decrease the expansion rate [15]. Theoretical and experimental investigations confirm that HIB milling technology can efficiently generate reproducible nano-

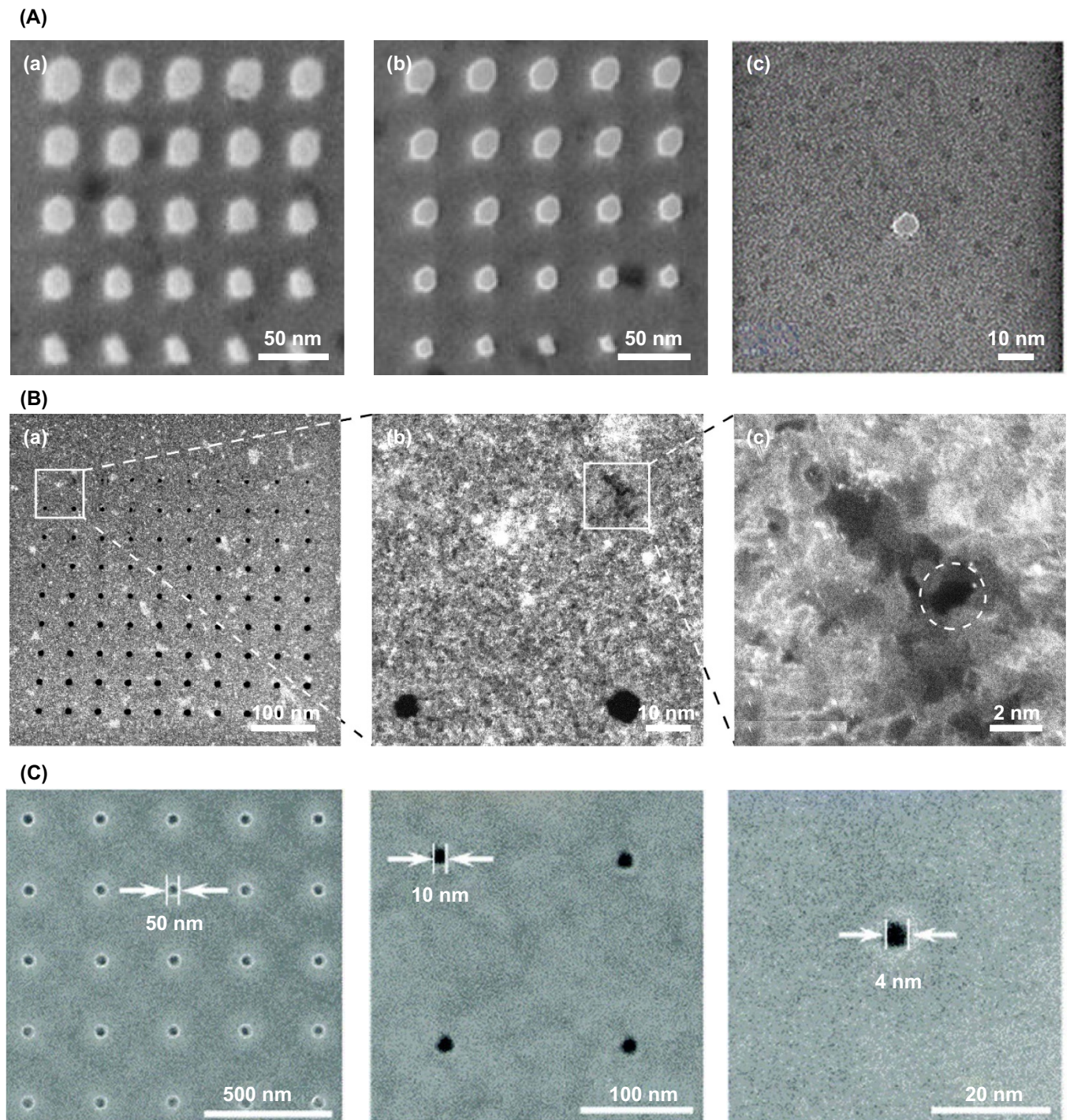


**Figure 4.** (A) Transmission electron micrographs of two nanopore arrays formed in different membrane thicknesses: (a)  $18.2 \pm 0.6$ , (b)  $13.7 \pm 0.6$  with the same range of  $\text{He}^+$  ion doses ( $0.4\text{--}7.1 \times 10^6$  ions/point). Scale bars are 50 nm [55]; (c) Representative transmission electron microscopy (TEM) image of a nanopore array with 0.3 s exposure time using an HIM. Republished with permission of the Royal Society of Chemistry from [14], permission conveyed through Copyright Clearance Center, Inc. (B) Scanning TEM images of nanopores in a CNM. (a) Overview of a spot exposure array. The dose increases from the top left to the bottom right corner. Bright patches result from residual polymers after the transfer. (b) The lower line pores received doses far beyond the breakthrough dose, while the upper line pores received doses at the breakthrough dose. The upper left position has no visible pores; at the upper right position, the dose ( $5.6 \times 10^5$  ions/point) is sufficient enough to create a defect in the membrane that is highlighted by a dashed circle in (c). Reprinted from [12], with the permission of the American Institute of Physics Publishing; (C) Nanopores on h-BN with diameters of 50 nm, 10 nm, and 4 nm, respectively. Republished with permission of the Royal Society of Chemistry from [57], permission conveyed through Copyright Clearance Center, Inc.

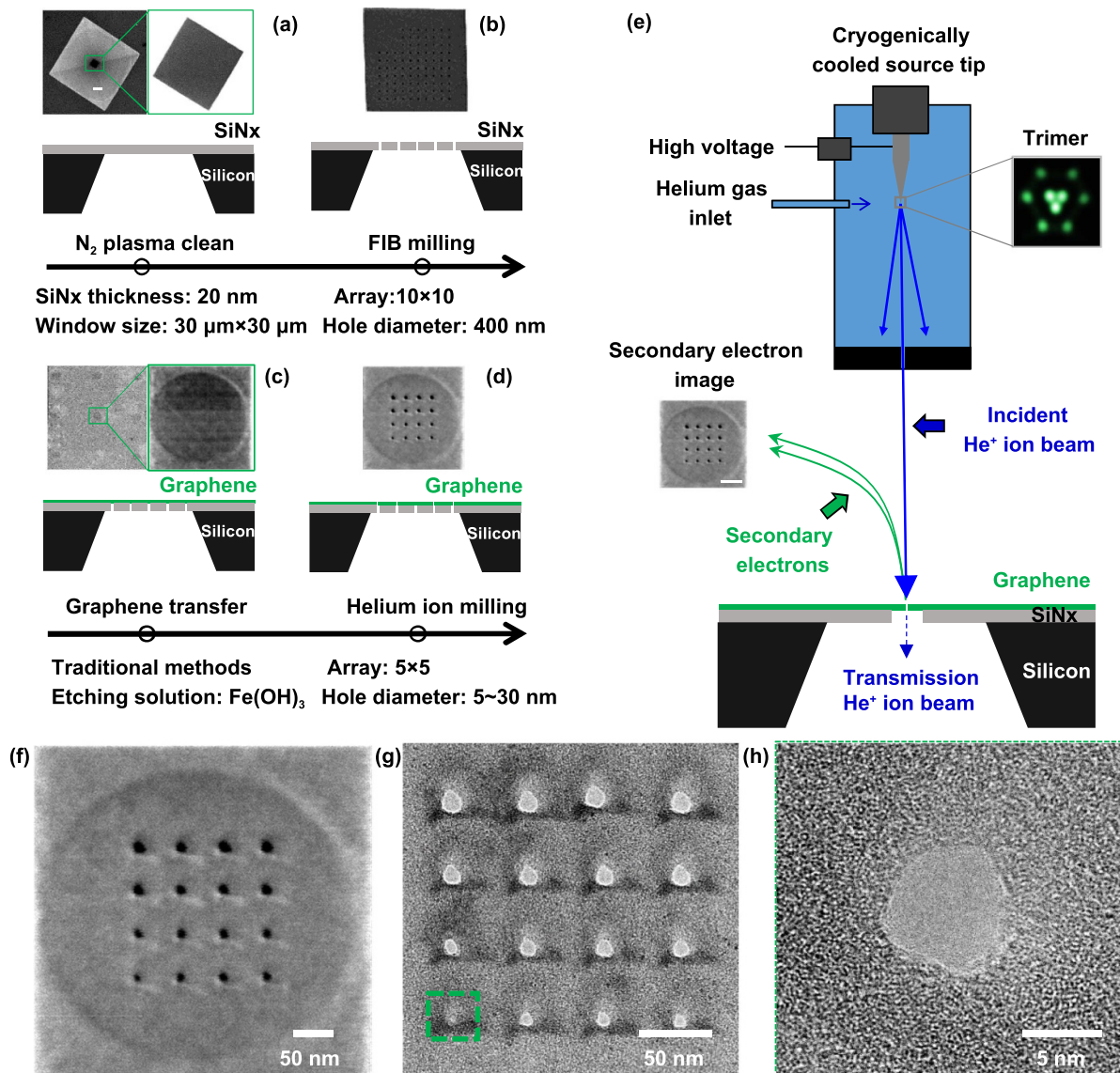


**Figure 5.** (a) Chip cleaning. (b) SiN<sub>x</sub> hole drilling by FIB. (c) Transferring graphene onto the FIB-drilled SiN<sub>x</sub> layer. (d) Graphene nanopore drilling by HIM technology. (e) Schematic diagram of graphene nanopore drilled using HIM. (f) HIM image of graphene nanopore drilled by HIM technology, the exposure time is 0.4~1.15 s from lower left to upper right; the step is 0.05 s. (g) TEM image of graphene nanopore array, corresponding to (f). (h) Magnified TEM image of a nanopore marked with a green square in (g), the mean diameter is approximately 5 nm. Modified with permission from [15]. Copyright 2016 Institute of Physics Publishing.

scale nanopore patterns on freestanding 2D graphene [62]. Moreover, the graphene nanomesh formed by patterning nanopore arrays directly through HIM milling in the suspended monolayer graphene has potential to control phonons, water filtration, and semiconductor applications [63].

#### 4.2. Milling for 3D nanostructures

In addition to nanopore fabrication, HIM milling can also be used to direct pattern other nanostructures, such as special 3D nanostructures and plasmon nanostructures. First, a set of parallel lines, 3D nanopyramid, and nanocone structures are patterned by HIM milling on a Si substrate, as shown in figure 6 [64]. The small focal spot size helps to confine the interaction between high-energy helium ions with Si. 3.5 nm half-pitch

parallel lines can be achieved by direct writing nanofabrication [65]. Unlike FIB milling based on gallium ions, when HIM bombardment is focused on a Si substrate, the implanted helium ions tumefaction leads the surface to swell. At the same time, Zhang L *et al* demonstrated that these nanostructures are stable at room temperature, which were generated through diffusion, coalescence, and nanobubble formation [64]. Furthermore, direct-write HIM milling is used to fabricate metrology test structures with programmed imperfections. Due to the high resolution of HIM, features around 5 nm are resolvable. The direct-write HIM milling process can then pattern 1.5 nm structures by correcting the proximity effect. It can offers a promising alternative method for fabricating programmed defects and test structures for sub-7 nm advanced metrology solutions [66, 67].

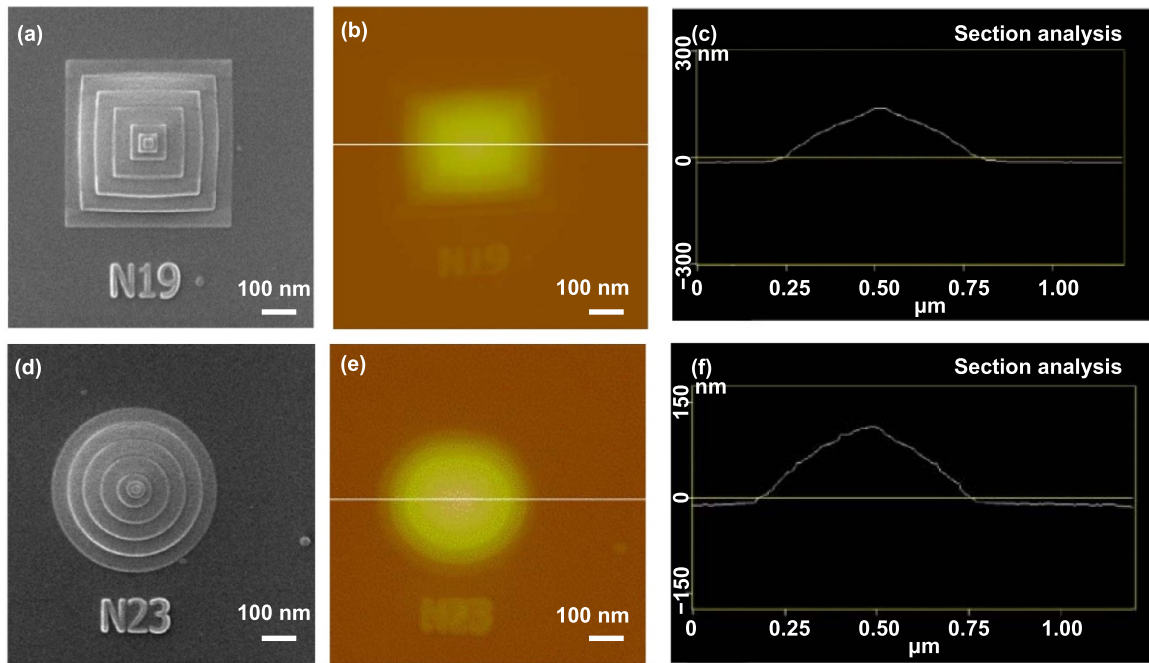


**Figure 6.** HIM images (top row), AFM images (middle row), and height profiles (bottom row) of (a)–(c) nanopyrramid and (d)–(f) nanocone obtained by HIM-patterning with dose gradients; Modified by permission from [64]. Copyright 2015 Institute of Physics Publishing.

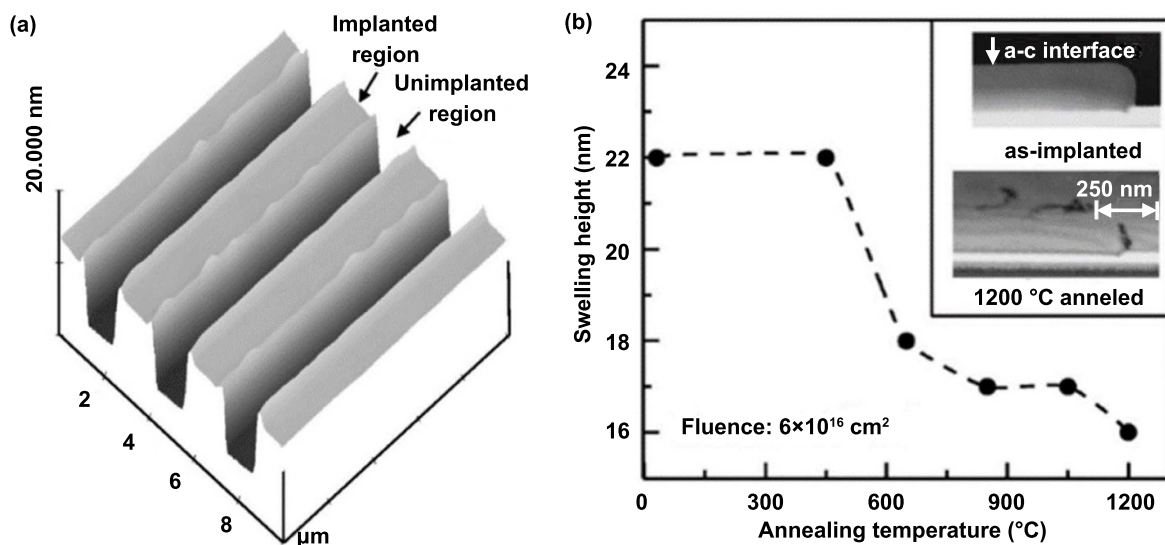


**Figure 7.** An AFM image of the swelling observed in 80 KeV  $\text{Si}^+$  implanted Si at room temperature, with fluence  $6 \times 10^{15} \text{ ions cm}^{-2}$ , as shown in (a). The un-implanted region corresponds to the masked region during implantation. (b) The saturated step height as a function of post-implantation isochronal annealing at various temperatures, shown for  $6 \times 10^{16} \text{ ions cm}^{-2}$  implanted sample. Inset shows the cross-sectional TEM images of the as-implanted and 1200 °C annealed samples, respectively. Reprinted figure with permission from [69]. Copyright (2001) by the American Physical Society.

#### 4.3. Swelling for specific nanopore fabrications

Helium ion bombardment in the HIB milling process can damage bulk materials, resulting in defects, such as bubbles, that have a significant impact effect on special applications. On the other hand, we can take advantage of the bubble phenomenon to form special nanostructures. Due to its high resolution, great depth of field, and minimal damage on the substrate, HIB

technology was used to create ultra-high aspect ratio vias and 3D nanovolcanic nanopores on gold film [68]. HIM imaging can characterize the feature size, lateral milling resolution, and sidewall angle for specific topography. The results show that in addition to physical sputtering, amorphization (i.e. swelling) is another key method of preparing nanostructures on crystalline substrates by the HIB milling process. Generally, amorphization occurs in the bombarded area when the



HIB dose is not sufficient enough to induce sputtering. During the amorphization process, the incident helium ions displace the target atoms from their lattice sites. The movement of displaced atoms relocating to the nearby areas expands the substrate.

Giri P K *et al* demonstrated the swelling mechanism of silicon irradiated by low energy ions through AFM and TEM experiments, as shown in figure 7 [69, 70]. For SiC at room temperature and low flux, the implanted helium ions relaxed the local strain, thereby promoting implantation. Leclerc S *et al* reported that the amorphization phenomenon contributes 15% of the thickness of the amorphous layer in the swelling process [71]. Tseng, A. A. also demonstrated that the maximum swelling range due to amorphization can reach tens of nanometers [72]. Therefore, we should consider amorphization in nanofabrication to control the dimensional accuracy of nanostructures. Swelling caused by amorphization has been used to form special nanostructures in HIB-milled gold films, such as nanovolcanic nanopores (figure 8), which have the potential to enhance fluorescence and scattered light in chemical sensing and biophysical applications [16, 68, 73]. Because of its light mass, helium ions propagated into the Au layer over a long distance, resulting in significant ion implantation, as shown in figure 8(g). The implantation of helium ions induced further swelling around the nanopore and formed 3D nanovolcanic nanopores. When the dose of HIB is  $10 \text{ nC } \mu\text{m}^{-2}$ , the height of fabricated 3D structures can reach about 50 nm (figure 8(f)), which is higher than the depth of the HIB milling process [16]. However, Marshall M M *et al* [54] suggests that the volcanic structures are the result of charge-induced fluidization of the material and ionic pressure.

## 5. HIB-induced deposition

Ion-beam-induced deposition is an important nanofabrication technology that can modify the properties of materials according to the interactions between the ion beam and the materials. The advantages of direct writing and growth make the deposition process useful for specific nanofabrication applications. Tseng A A recently reported that by adding GIS in the chamber, gallium FIB induced deposition has been widely used in circuit editing, device modification, and nanoelectronic device fabrication [72]. Following the scanning ion beam, the deposition process occurs in the interaction between the volatile compounds (e.g. organometallic, halides, and halogenides), the gaseous precursor, and the target material in the vacuum chamber. The gaseous precursors are physically adsorbed on the target substrate and then locally dissociated by the high-energy scanning gallium ion beam where the ion beam strikes the substrate. Following Moore's Law, the scale of integrated circuits have progressively increased with the development of semiconductor technology. However, gallium FIB-induced deposition technology cannot meet the nanofabrication requirements of future circuit editing and nanoelectronic devices fabrications due to its problems, because the resolution of the gallium

ion beam is low and the substrate could be damaged by the exposure of gallium ion beam. The development of HIB-induced deposition is a reasonable, appropriate technique for these specific nanofabrication applications because of the light mass of helium ions and the different electrical properties between inert helium and electroactive gallium [8, 9, 17, and 74]. This chapter outlines the latest work on HIB-induced deposition.

### 5.1. Deposition parameters optimization and model simulation

When HIB scans gaseous precursors at the substrate surface, the competition between physical and chemical kinetics induces metal deposition on the substrate. The chemical reaction rate of the gaseous precursor under HIB exposure is greater than the removal rate of parasitic material from the substrate by HIB bombardment. The deposition rate strongly depends on the precursor gas coverage of the substrate surface in HIB-induced deposition. The shape and volume of the deposit on the substrate varies with the competition between deposition and sputtering processes, the thermal and beam-enhanced diffusion, and the implantation of primary ions. Shadowing—which results from partial exposure to the precursor flux—has a specific effect on the shape and volume of the deposit. Therefore, it is necessary to optimize the deposition parameters of a specific nanoprocess for HIB-induced-deposition technology. Initially, Alkemade P F group achieved HIB-induced Pt deposition using a Carl Zeiss ORION™ HIM equipment with OmniGIS [75, 76]. For Pt deposition with (Methylcyclopentadienyl) trimethyl platinum ( $(\text{CH}_3)_3\text{Pt}(\text{C}_p\text{CH}_3)$ ) as the gaseous precursor, various controllable parameters such as beam current, beam overlap, and deposition size were investigated. Statistical experiments show that during HIB-induced Pt deposition, HIB current, scanning pixel pitch, and total deposit size have a significant effect on the metal deposition rate and composition (figure 9(a)) [77].

Alkemade P F *et al* also demonstrated that the growth of nanopillars via HIB-induced deposition strongly depends on the consumption of gaseous precursor molecules [78]. Compared to continuous HIB exposure, the pulsed HIB-induced deposition was developed as a new nanofabrication method. Pulsed HIB can reduce depletion, thereby increasing the growth rates of PtC nanopillars. The high growth rate and rapid vertical growth produced nanopillars with high aspect ratios. The deposition efficiency of short dwell times is 20 times higher than that of continuous HIB exposure conditions. The non-damaging dose optimizes the parameters of the HIB-induced deposition process to reduce the damage caused by high-energy helium ion bombardment [79]. The proximity effect—which is caused by charging or discharging neighboring structures—causes the deposited pillars to grow both vertically and laterally as the pitch decreases [8]. Ultimately, the optimization of HIB-induced deposition process parameters, such as beam current, dwell time, beam focus, and refresh time of gaseous precursor, is necessary

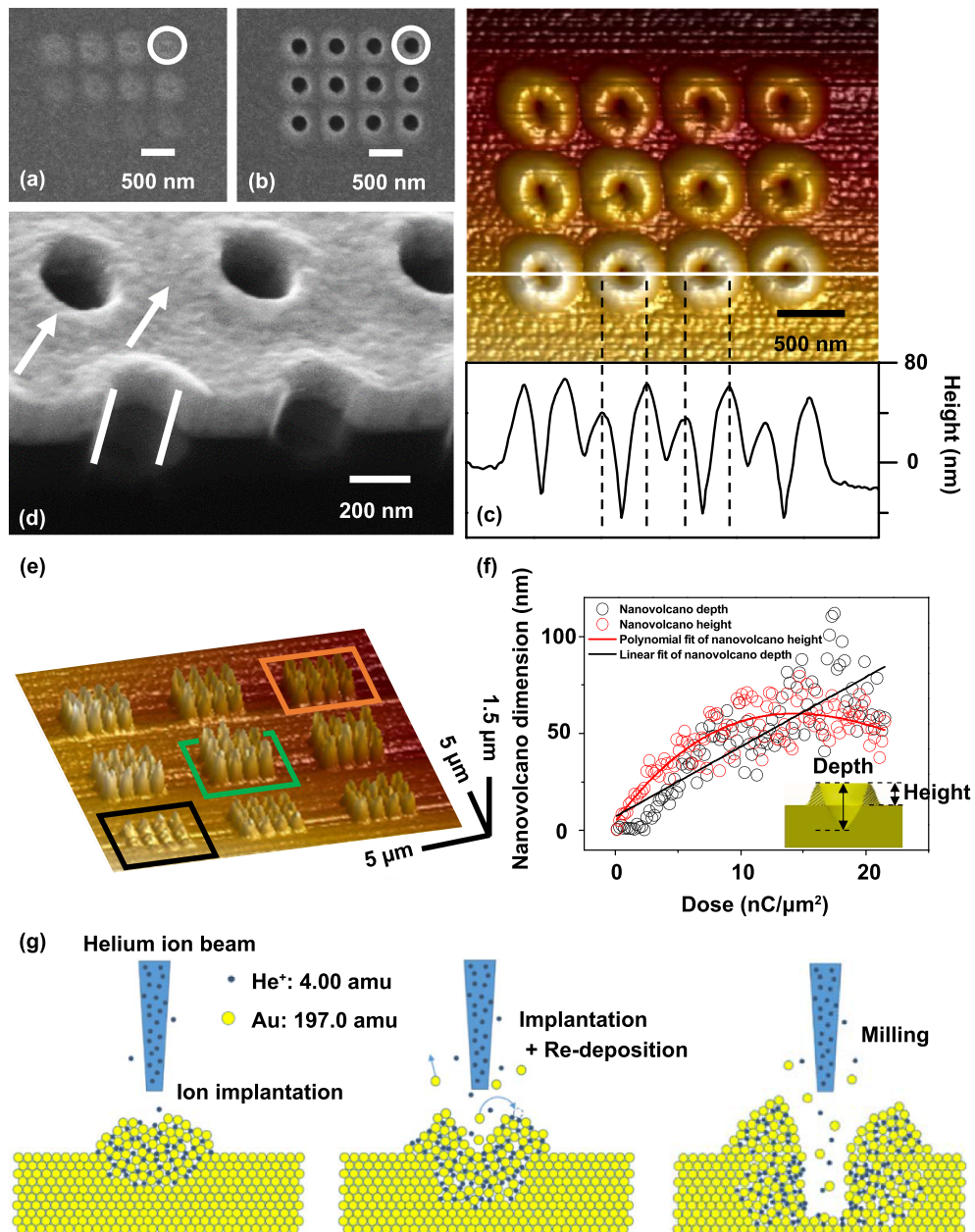


**Figure 8.** Nanovolcano-shaped nanopore arrays milled with helium ion beam: [(a), (b)] HIM images for helium ion doses of (a) 0.1–2.3 and (b) 4.9–7.1  $\text{nC } \mu\text{m}^{-2}$ ; (c) AFM image and corresponding height profile of the nanopore made with a dose the same as in (b); (d) cross-sectional AFM image; (e) AFM images of nanovolcano-shaped nanopores fabricated using HIM with a dose ranging from 0.1–21.5  $\text{nC } \mu\text{m}^{-2}$  and a step of 0.2  $\text{nC } \mu\text{m}^{-2}$ . (f) nanopores milled by helium ion beams. (Inset) Image showing the height and depth of nanovolcano-shaped nanopore; (g) Schematic diagram of the formation process of nanovolcano shaped nanopores made with a small, moderate, or large dose of helium ions. Reprinted from [16], with the permission of the American Institute of Physics Publishing.

to efficiently and precisely fabricate extended, complex nanostructures.

The simulation of HIB-induced deposition qualitatively reflects the relevant processes that guide extreme nanofabrication. In this article, both Monte Carlo simulation and analysis models are used to quantify and understand the complex processes involved in HIB-induced deposition [80]. Taking the fabrication of nanopillars deposited by HIB-induced deposition as an example, the competition between helium ions, SE, and dispersed ions in the vertical and horizontal

column, induced nanopillar growth nanopillars, as shown in figures 9(b) and (c) [76]. When  $(\text{CH}_3)_3\text{Pt}(\text{C}_2\text{H}_5)_3$  is used as the gaseous precursor, the growth rate of PtC pillars is related to the HIB beam current. The Monte Carlo simulation of HIB-induced deposition also shows that the reaction rate can affect the vertical growth and the lateral broadening with incident primary helium ions [81]. However, due to the scattered ions and SEs, the proximity effect limits mass transport, which decreases the vertical growth velocity but broadens the deposition structures. The Monte Carlo simulations were

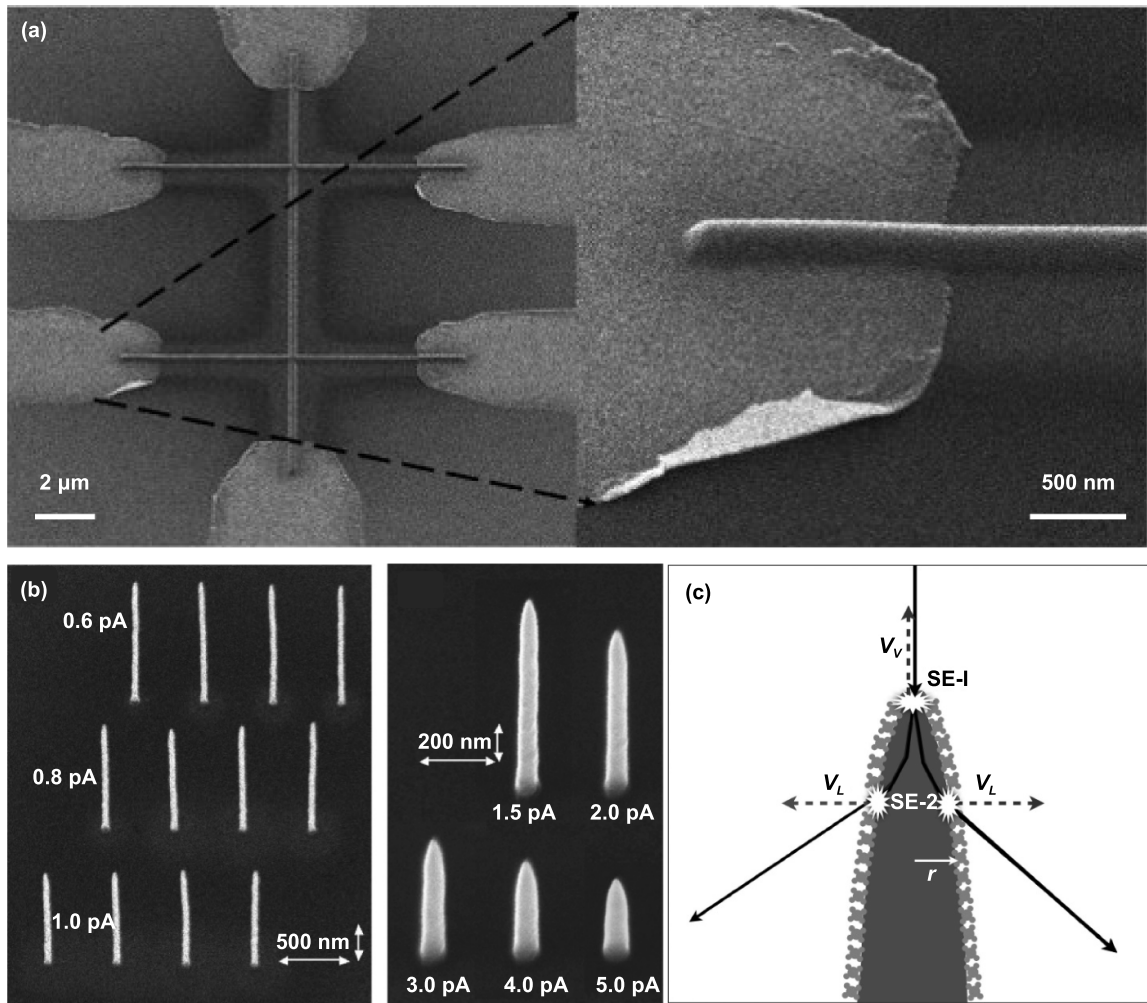


**Figure 9.** (a) Scanning HIB micrographs of HIB-induced deposition deposited devices prepared for temperature-dependent electrical conductivity measurements. Reprinted with permission from [77]. Copyright 2013 Institute of Physics Publishing. Pillars grown with 25 keV  $\text{He}^+$  beams at various currents, as shown in (b). The dose is 6.0 pC. Pillars grown at the lowest current are highest and thinnest. (c) Sketch of a simplified model for HIB-induced deposition pillar growth. The incident ions and their related SEs of type 1 (SE-1) cause vertical pillar growth at a rate of  $v_v$ . The outgoing scattered ions and their related SEs of type 2 (SE-2) cause lateral growth at a rate of  $v_L$ . Growth rates depend on the level of precursor depletion at the apex, which in turn depends on the ion current. Reprinted from [76], with the permission of the American Institute of Physics Publishing.

carried out with actual values obtained from HIB-induced Pt deposition to predict the growth characteristics of PtC nanopillars [82].

### 5.2. Nanopillars deposition with different gaseous precursors

Ion beam-induced deposition of different nanostructures depends on the nature of the injected gaseous precursors and noble gas ion beams. Various gas compounds have been reported for focused gallium ion beam [73] and electron beam [9] induced deposition processes. Due to the different electrical properties of the inert helium and electroactive gallium, only a small amount of volatile compounds like organometallics were selected as gaseous precursors for HIB-induced deposition. Among them,  $(\text{CH}_3)_3\text{Pt}(\text{C}_p\text{CH}_3)$  was first used as a gaseous precursor to fabricate nanopillars with the HIB-induced deposition process [75]. The parameter optimization and theoretical simulation of HIB-induced Pt deposition make

it possible for nanofabrication of future circuit editing and nanoelectronic devices.

Other gaseous precursors aside from  $(\text{CH}_3)_3\text{Pt}(\text{C}_p\text{CH}_3)$ , such as  $\text{W}(\text{CO})_6$  and dicobalt octacarbonyl ( $\text{Co}_2(\text{CO})_8$ ), are used in the HIB-induced deposition process. Kohama K *et al* successfully deposited 40 nm wide and 2  $\mu\text{m}$  tall W-based pillars on carbon and silicon substrates using  $\text{W}(\text{CO})_6$  as the gaseous precursor for the HIB-induced deposition process [83]. Their experiments suggest that at least three phenomena occur during the formation of W-based pillar under HIB exposure: pillar deposition, sputter-etching, and Si blistering [83]. Wu H *et al* selected  $\text{Co}_2(\text{CO})_8$  as the gas precursor for HIB-induced Co nanowire deposition induced [84]. The resistivity and contact resistance of the deposited nanowire between the metal nanowire and the electrical substrate verify the feasibility of depositing high-quality Co metal lines through the gaseous precursor  $\text{Co}_2(\text{CO})_8$  using HIB-induced deposition.

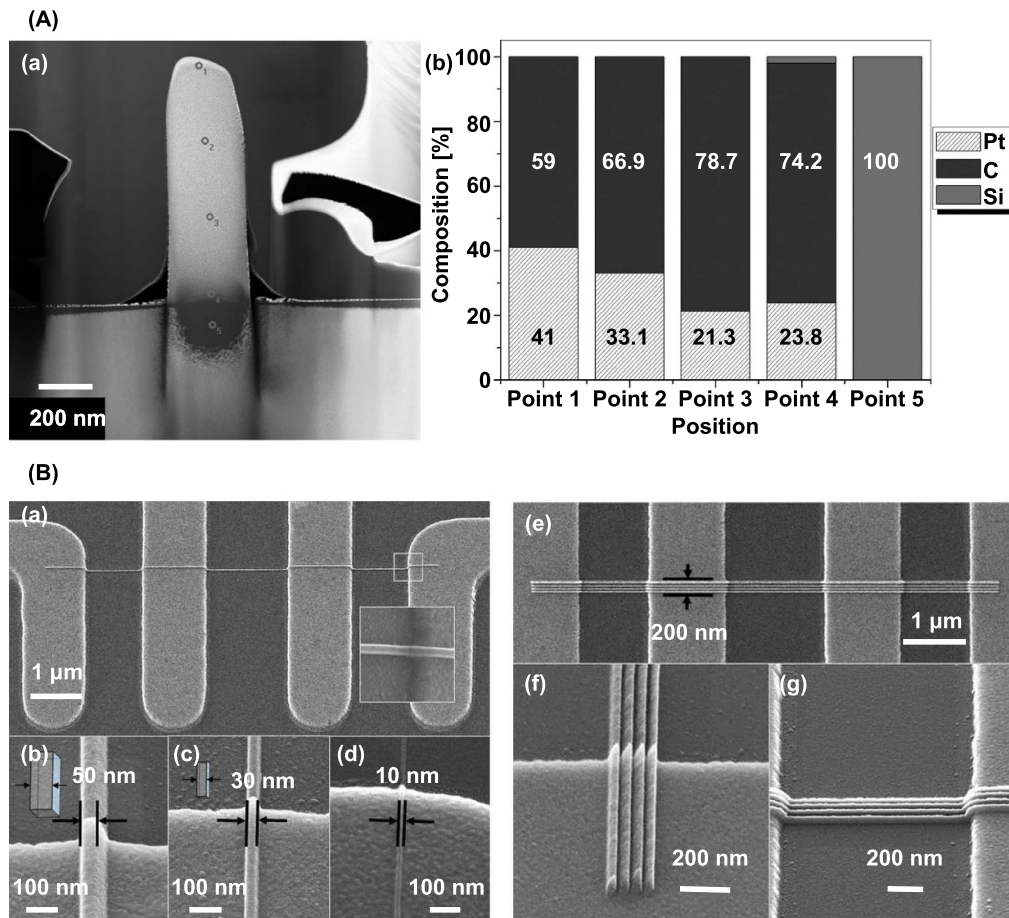


**Figure 10.** (A) TEM EDS point measurements taken along the deposited Pt pillars: (a) present the point locations and (b) present the composition analysis for the 0.1 pA deposition currents. Reprinted from [19], with the permission of the American Institute of Physics Publishing. (B) HIM images of He ion beam induced single cobalt line depositions with various line widths on 4 point probe test (ppt) structures: 50 nm (b), 30 nm (a) and (c), and 10 nm (d). (a) shows a Co line with 30 nm width and 10  $\mu\text{m}$  length on 4 ppt. The inset shows the good step coverage. (b)–(d) show higher magnification HIM images of 50 nm, 30 nm, and 10 nm Co lines. The insets in b and c are 3D schematic drawings of Co lines; (e) HIM images of a 4 line pattern with a 25 nm half-pitch (top view); (f) and (g) are 45° tilted angles high-resolution HIM images of this deposit with different rotations. Reprinted with permission from [Springer Nature Customer Service Centre GmbH]: [Springer Nature] [Journal of Materials Science: Materials in Electronics] [84], [COPYRIGHT] 2014.

### 5.3. Nanowire deposition for circuit editing application

Circuit editing is a powerful technique, widely used in the field of integrated circuits, to rapidly debug and modify nano-electronic devices. In conjunction with GIS, HIM is used to deposit complex patterns of sub-10 nm metals to fill and wire connections on the surfaces of nanoelectronic devices, due to its ultimately smaller probe size and beam profile with much less beam tail contribution. The purity of the deposited metal is high enough to achieve the low resistivity required in circuit editing applications. Drezner *Y et al* characterized the pillar morphology, structure, and composition of HIB-induced deposited metal by using TEM and energy dispersive spectroscopy (EDS) [19]. The maximum Pt content for HIB-induced deposition on the Si substrate was 41% (figure 10(A)). A lower HIB current is suitable for metal deposition because it involves less subsurface damage to the Si substrate in future circuit editing applications. The Co nanowires are deposited on the electrical test structure using the HIB-induced deposition process with the gaseous

precursor  $\text{Co}_2(\text{CO})_8$ . The extremely small spot size of HIB allowed for the effective patterning of single and multiple Co lines with 10 nm resolution by a scanning HIM equipment with Omniprobe GIS, as shown in figure 10(B). Good repeatability was obtained in the deposition of Co metal wires, and their purity was extremely high. HIM imaging, high-resolution TEM imaging, and electron energy-loss spectroscopy also show that there was almost no overspray around the deposition area [84]. The investigation of deposit composition and the subsurface damage with HIB-induced deposition in sub 10 nm patterns fabrication at high densities provides a new solution for future circuit editing application.

Owing to its excellent electrical properties, graphene has been chosen as a new material to fabricate next generation nanoscale electronic devices. In the case of HIB-induced deposition, W and Pt wires are deposited on graphene nanodevices assisted with gaseous precursors, forming an electrical contact in quantum cellular automaton devices [85]. Since the deposition rate is a function of the HIB current, the growth of deposition wires is related to the dose of helium

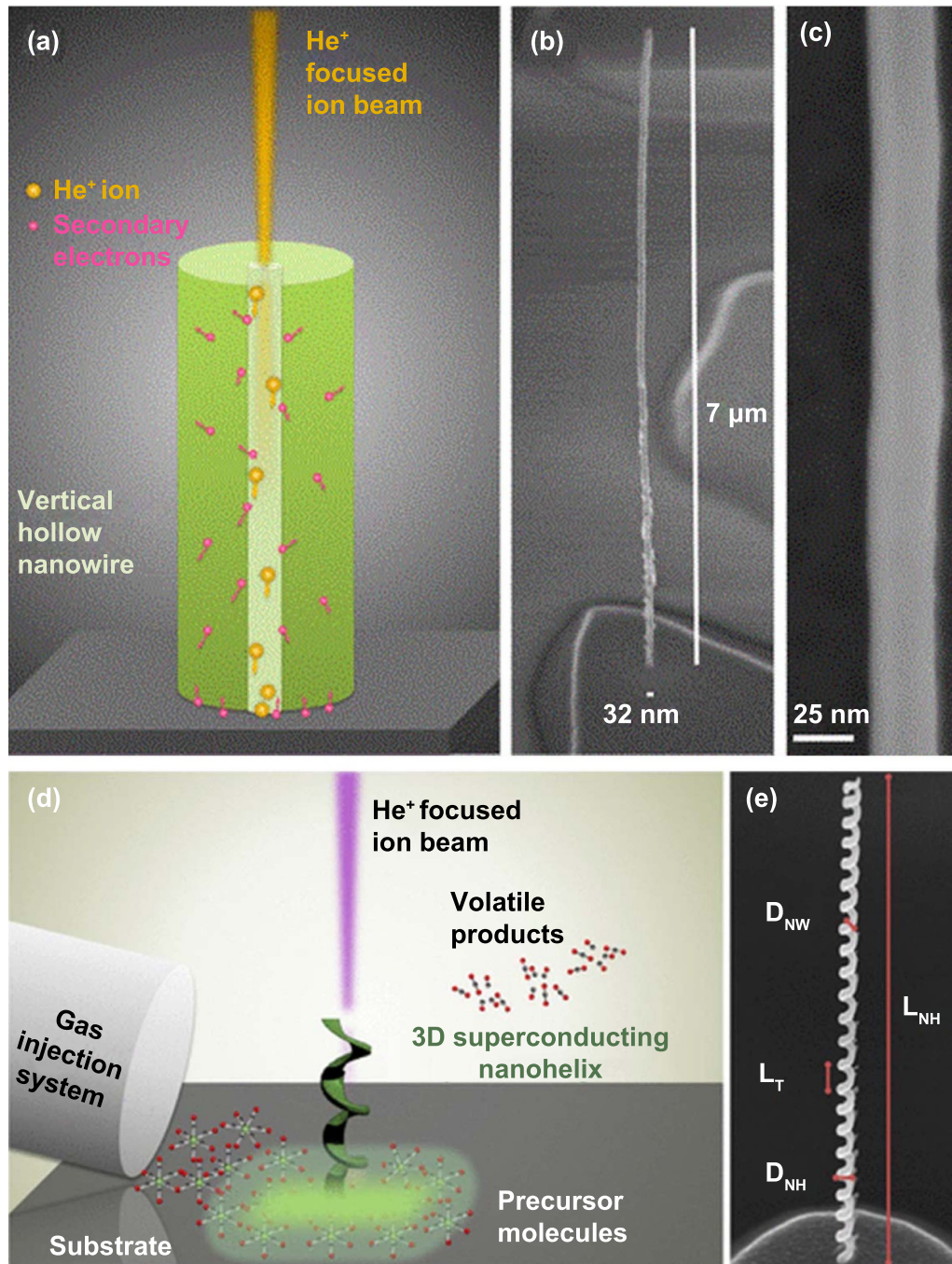


**Figure 11.** (a) Vertical growth of WC hollow nanowire using a HIB focused to  $\sim 1$  nm. (b) SEM image of a vertical 3D WC hollow nanowire ( $52^\circ$  tilted stage). (c) High-magnification SEM image of the WC nanowire. Reprinted with permission from [65]. Copyright 2018 American Chemical Society. (d) Sketch of the growth of 3D nanohelix by HIB-induced deposition; (e) SEM image of a WC 3D nanohelix of type 1, in which pattern parameters are indicated,  $D_{NW}$ : nanowire diameter,  $D_{NH}$ : nanohelix diameter (100 nm in this specific case),  $L_T$ : turn length or pitch, and  $L_{NH}$ : nanohelix length ( $52^\circ$  tilted stage). The specific deposition parameters for the helix are as follows: beam current  $\approx 1$  pA, beam spacing = 10 nm, nominal diameter = 75 nm, beam dwell time = 700 ms, and turns = 23. Reprinted with permission from [87]. Copyright 2019 American Chemical Society.

ions. HIB direct writing can also be used to directly pattern graphene without significantly damaging the substrate. Therefore, the combination of HIB direct writing with HIB-induced deposition can fabricate subnanometer-scale graphene nano-electronic devices with optimized process parameters.

Superconducting W nanowires grown by HIB-induced deposition technology are used in hybrid coplanar waveguide microwave resonators, which are combined with sputtered niobium thin films in high-frequency superconducting circuits [86].

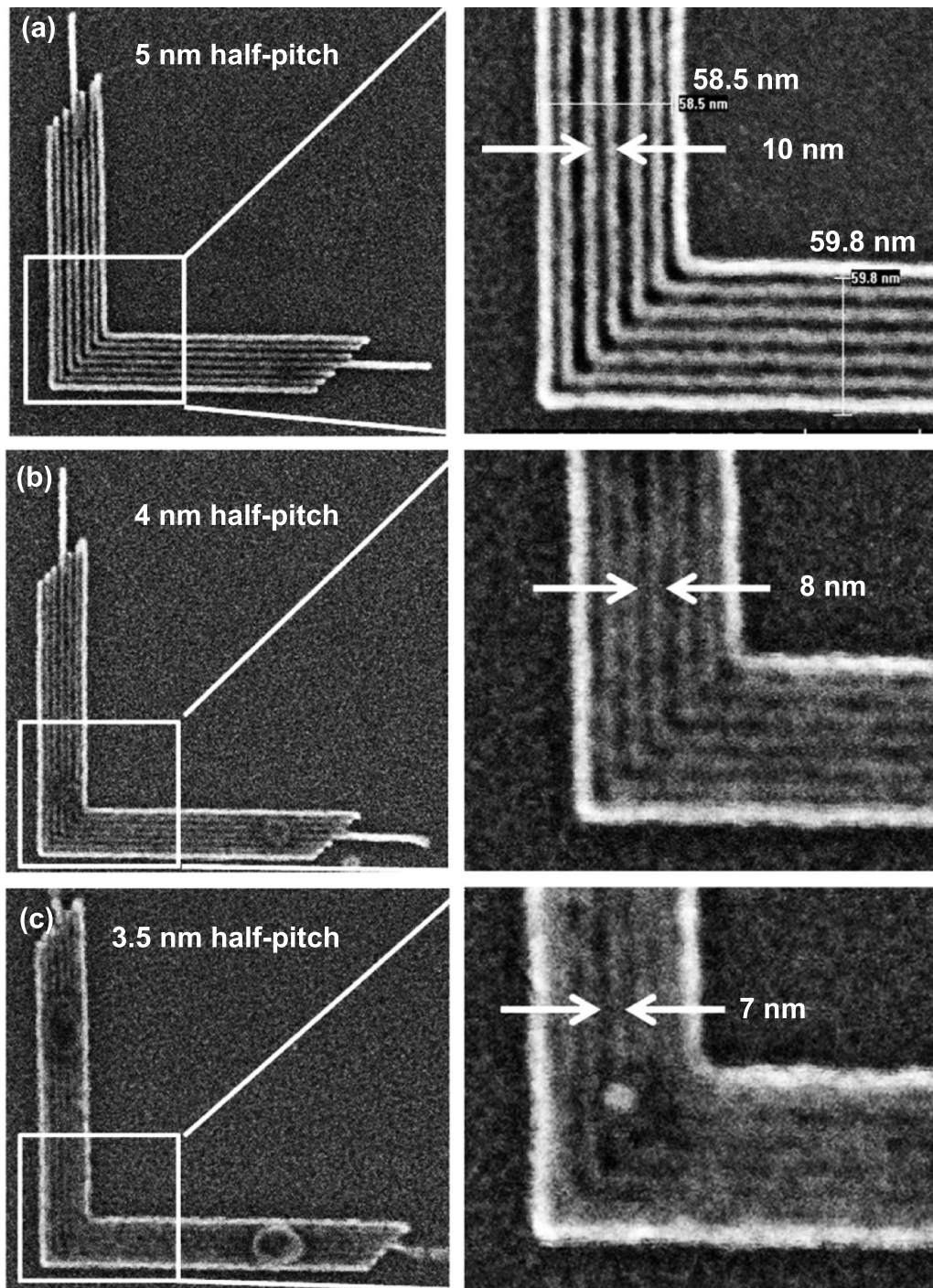


**Figure 12.** SEM images of (a) 5 nm, (b) 4 nm, and (c) 3.5 nm half-pitch nested L's formed by helium ion beam lithography in an HSQ layer that was subsequently developed to remove the unexposed resist. Five nanometers and 4 nm half-pitch patterns were resolved. Although the 3.5 nm half-pitch patterns were not completely resolved, there were regions in which individual lines are distinct. Reprinted with permission from [92]. Copyright 2012 American Vacuum Society.

#### 5.4. 3D nanostructures deposition for nanoelectronic devices fabrications

Córdoba R *et al* first fabricated 3D superconducting W carbide (WC) hollow nanowire with a diameter of 32 nm and a maximum aspect ratio (length/diameter) of 200 by using the HIB-induced deposition technique with the gaseous precursor  $W(CO)_6$ , as shown in figures 11(a)–(c) [65]. Because of

their quasi-one-dimensional superconductivity, the fabricated nanowires demonstrated a large critical magnetic field and current density when they were superconducting at 6.4 K. As shown in figures 11(d)–(e), through the direct writing method, Córdoba's team also fabricated novel 3D WC nanohelices by controlling key deposition parameters for superconducting applications. Córdoba R *et al* experimentally identified the characteristics of the vortex and phase-slip

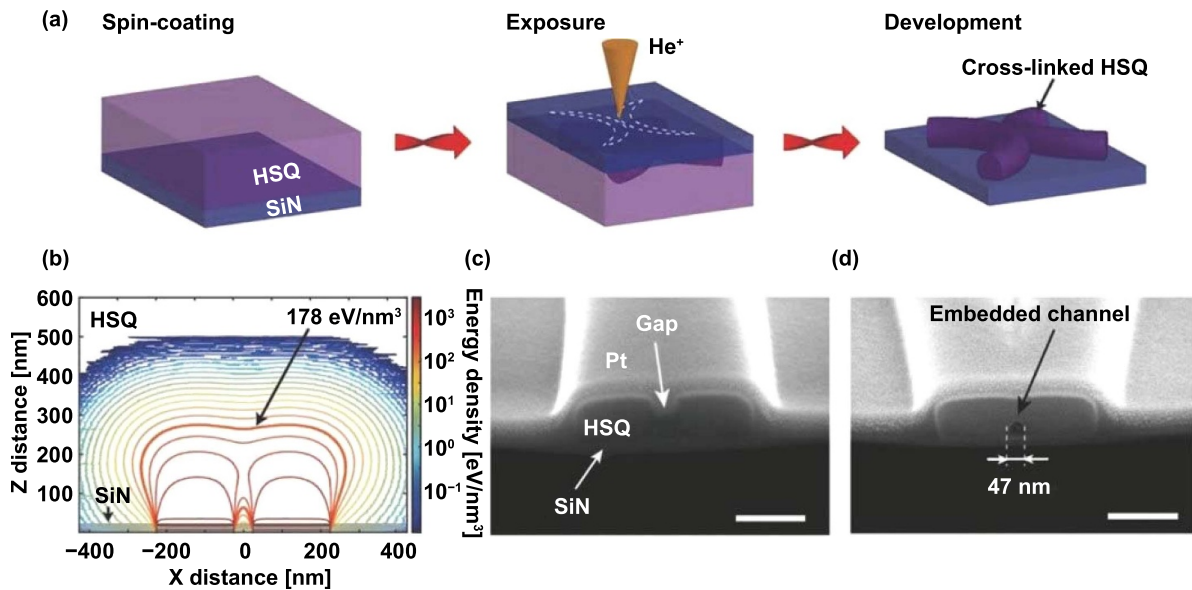


**Figure 13.** Through-membrane 3D fabrication of crosslinked hollow nanostructures in HSQ. (a) Schematic of the through-membrane fabrication of an embedded HSQ nanochannel by exposing two curved stripes with a small gap in between. (b) Vertical cross-sectional contours of deposited energy density for a  $\text{He}^+$  dose of  $600 \mu\text{C cm}^{-2}$ . The exposure pattern consists of two 200 nm wide and  $1 \mu\text{m}$  long curved stripes separated by a gap of 50 nm. The shown cross-section is at the center of the stripes. (c and d) SEM images of cross-sections cut by a gallium FIB, showing in (c) the separated HSQ stripes at a position off-center and in (d) a channel embedded at the center by HSQ, where the exposure gap is 47 nm. The scale bars in (c) and (d) represent 200 nm. Reprinted with permission from [98]. Copyright 2018 John Wiley and Sons.

patterns based on its helical 3D geometry, which induces specific superconducting properties [87]. The advantages of using HIB-induced complex 3D nanofabrication methods provide more opportunities for nanoelectronic devices based on other sophisticated 3D nano-superconductors.

## 6. Additional HIB nanofabrication

Electron beam lithography (EBL) is a supplement to photolithography and one of the most well-established technologies for fabricating prototype nanoelectronic devices through top-down processes. Focused electron beams can modify the chemical properties of thin resist materials coated on substrates into which the arbitrary pattern nanoscale structures are created upon exposure [88]. Due to its sub-nanometer spot-size, the focused HIB is a new, high-resolution direct writing exposure beam for nanofabrication. Considering its high resolution, high SE yield, and low proximity effect, HIB direct writing is equal to or better than EBL for nanoelectronic devices fabrication. Moreover, helium ions have relatively low mass and are less damaging to target substrates compared to other particles, such as electrons and gallium ions [89, 90]. Therefore, the HIB direct writing technique can be considered as a new alternative ‘bottom-up’ nanofabrication method.

### 6.1. Resist assisted nanostructures

Resist assisted HIB direct writing uses a focused HIB to modify chemical properties of resist materials and to alter the solubility of the exposed resist. The subsequent development

step with a chemical solvent is carried out and a topographical pattern can be formed in the resist. The minimum feature size achievable with resist assisted HIB direct writing depends on the interaction of HIB with the resist and its properties. The focused HIB with a sub-nanometer spot-size and GFIS produces high-resolution direct writing comparable to or superior than that achieved with electron beams. Many resist materials demonstrate their potential for use in HIB direct writing owing to their ability to be patterned down to  $\sim 10$  nm or less.

Shi X and Kalhor N *et al* discussed and reviewed the HIB-resist interaction mechanisms and the latest experimental results using HIB direct writing with resist assistance [20, 91]. By combining high-resolution HIB patterning and nanoimprint lithography Li W D *et al* [92] fabricated a series of sub-10 nm line patterns with 4 nm half-pitches by exposing a layer of hydrogen silsesquioxane (HSQ) resist with a scanning focused HIB, as shown in figure 12. A novel, negative tone fullerene-derivative molecular resist was investigated with HIB direct writing to fabricate sparse line features with 7.3 nm line widths using standard processing conditions with minimal proximity effect [93]. The isolated features as small as 5 nm were patterned using focused HIB direct writing with a recently developed alumina-based negative-tone resist. The alumina-based resist was synthesized using a sol-gel method that nearly turned into a completely inorganic alumina system when exposed to the ion beam [94]. In field-emission device fabrication, a negative tone metal-organic (MOC) resist was presented which can be patterned to produce sub-10 nm features on a sub-20 nm pitch in Si and W when exposed to HIB direct writing at line doses on the order of

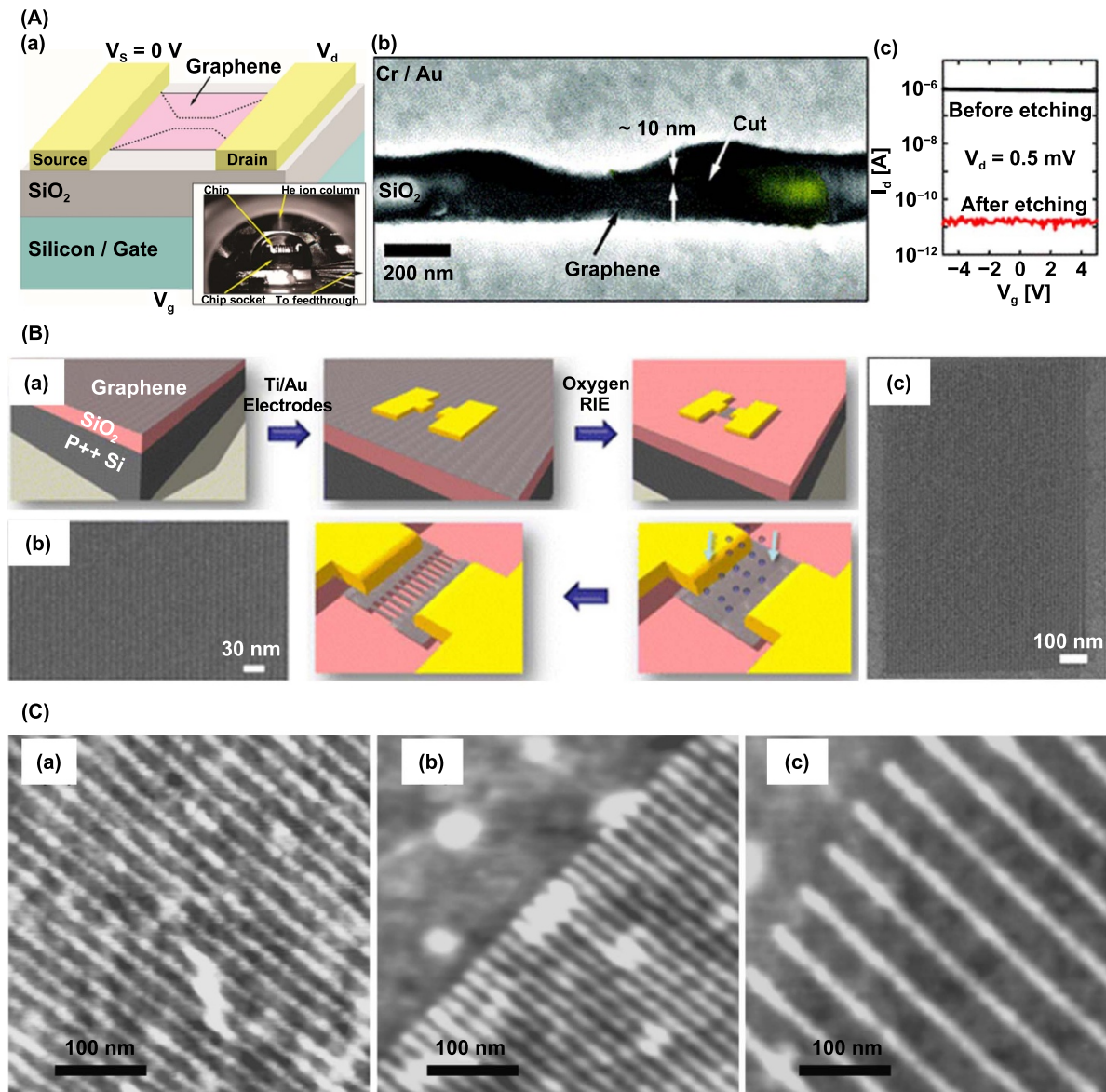


**Figure 14.** (A) (a) Schematic of a graphene device. Inset: photograph of the microscope chamber with an installed chip. (b) HIM image (with false color, cross-section viewing) of a suspended graphene device after etching with minimum feature sizes of about 10 nm. (c) Electrical measurement of the device before and after etching. Reprinted with permission from [13]. Copyright 2009 American Chemical Society. (B) (a) Scheme of graphene nanoribbon arrays fabricated by HIB lithography. (b) Helium ion microscope image of 5 nm half-pitch arrays. (c) HIM image of high aspect ratio graphene nanoribbons (width  $\times$  length is 5 nm  $\times$  1200 nm). For all images, bright lines represent graphene. Adapted with permission from [22]. Copyright 2014 American Chemical Society. (C) AFM topographic images of graphene nanoribbon superstructures with different distances between defect lines: (a)  $25 \pm 4$  nm; (b)  $20 \pm 4$  nm, (c)  $50 \pm 4$  nm. In all cases, the average width of the defect lines is  $5 \pm 4$  nm. The images were carried out using a Nano Wizard AFM (JPK) operated in intermittent contact mode. Reprinted from [100], with the permission of the American Institute of Physics Publishing.

tens of pico coulombs per centimeter [95]. A negative tone resist incorporating nickel-based MOC clusters (Ni-MOC) was investigated under HIB direct writing for the first time. High-resolution  $\sim 9$  nm line patterns were well developed at a sensitivity of  $22 \mu\text{C cm}^{-2}$  and significantly lower line-edge/width roughness of  $1.81 \pm 0.06$  nm and  $2.90 \pm 0.06$  nm. These findings elucidate the potential for sub-10 nm technology nodes, under standard processing conditions [96].

The ultimate resolution of lithographic features depends on both the point-spread function and resist contrast. The proximity effect is reduced to a single-digit nanometer resolution

for single-pixel exposures over small areas. Flatabo R *et al* showed that HIB direct writing can fabricate precision high-density gratings on  $100 \times 100 \mu\text{m}$  planar surfaces with a pitch as small as 35 nm using an area dose for exposure without any proximity effect corrections while maintaining a large focus tolerance [97]. The proximity effect due to the interaction between the high-energy HIB and the resist, and the lithographic effect at sites nearby the original beam incidence site can be exploited for nanofabrication.

As shown in figure 13, Cai J *et al* experimentally investigated the 3D interaction volume between incident



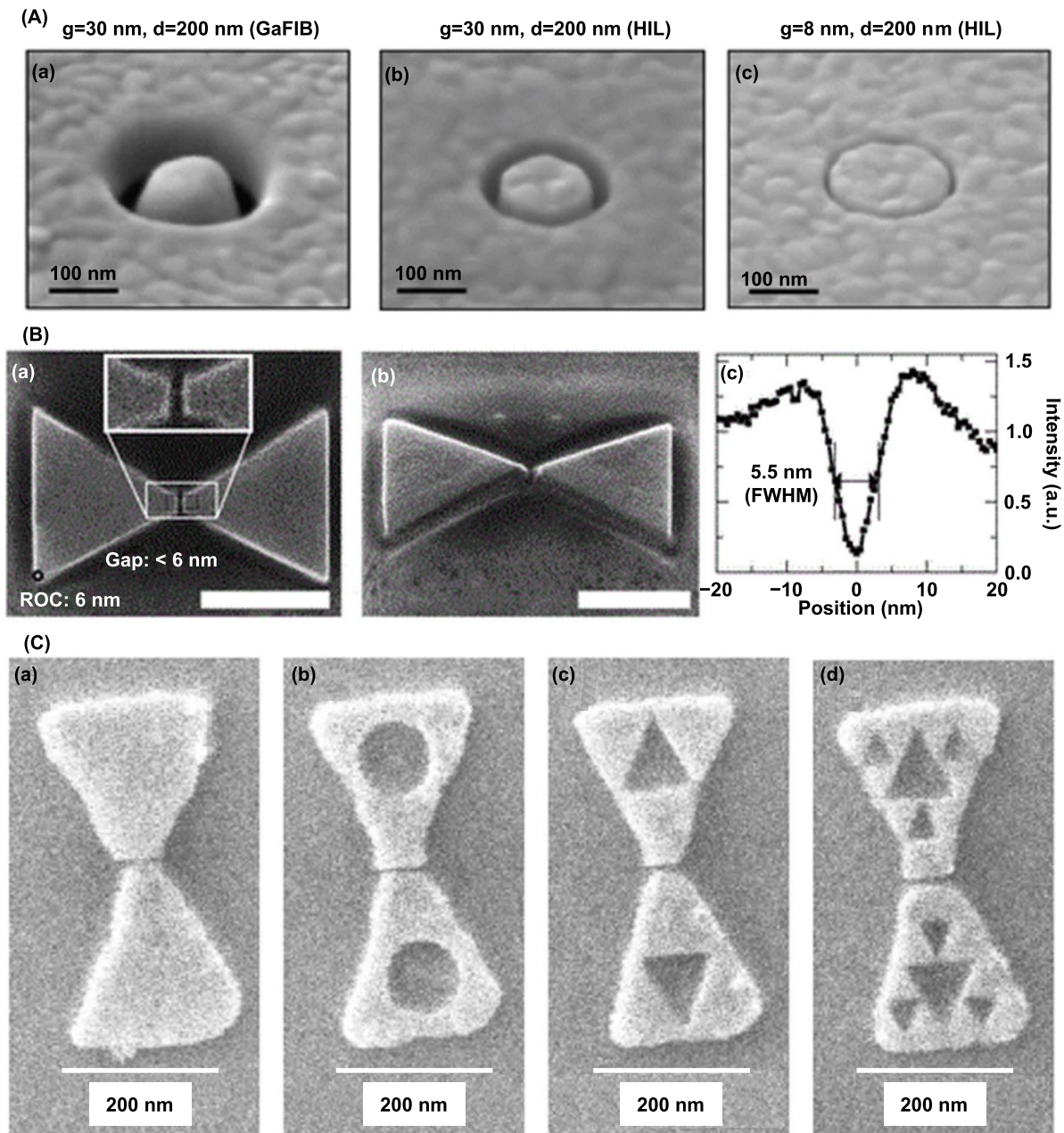


**Figure 15.** (A) SEM images of coaxial apertures with 200 nm diameter in a 100 nm thick gold film. (a) Coax made with gallium FIB with a nominal gap of 30 nm. (b) Coax made with helium ion lithography (HIL) with a nominal gap of 30 nm. (c) Coax made HIL with a nominal gap of 8 nm. Reprinted with permission from [104]. Copyright 2013 American Chemical Society. (B) HIM (a) and (b) images of bowtie nanoantennas fabricated by  $\text{He}^+$ -ion beam milling. All antennas are milled into a 30 nm thick polycrystalline gold film evaporated onto a glass substrate. (a) Bowtie antenna fabricated by  $\text{He}^+$  milling. A considerably reduced gap size of less than 6 nm and much sharper corners ( $\text{ROC} \leq 6$  nm) are obtained. (b) Side view of the same antenna (tilt angle  $35^\circ$ ) showing the excellent aspect ratio reached by  $\text{He}^+$  milling. (c) Cross-section through the gap region of the image in (a), indicating a gap width of 5.5 nm. All scale bars are 200 nm long. Reprinted with permission from [23]. Copyright 2014 American Chemical Society. (C) Bowtie structures fabricated by EBL and focused HIB milling imaged with the HIM. (a) Bowtie with  $\text{He}^+$ -beam cut the gap, (b) bowtie with cut-out circles and gap, (c) first-order fractal bowtie, and (d) second-order fractal bowtie. Reprinted with permission from [107]. Copyright 2019 Institute of Physics Publishing.

helium ions with HSQ [98]. They developed a new, flexible 3D nanofabrication technique by using a novel through-membrane exposure method of HIB direct writing. The 3D volumetric energy deposition of incident helium ions and its local crosslinking with HSQ under focused HIB exposure enable the fabrication of complex crosslinked HSQ nanostructures, such as embedded nanochannels and suspended

grids. The proposed crosslinked HSQ method expands normal HIB into 3D lithography for nanofabrication. HIB direct writing can also be used to pattern other nanostructures without the aid of resists, such as special graphene devices and plasmon nanostructures. Thereafter, we discuss the non-resist-assisted HIB direct writing technology and its nanofabrication applications, which offer rapid device prototyping

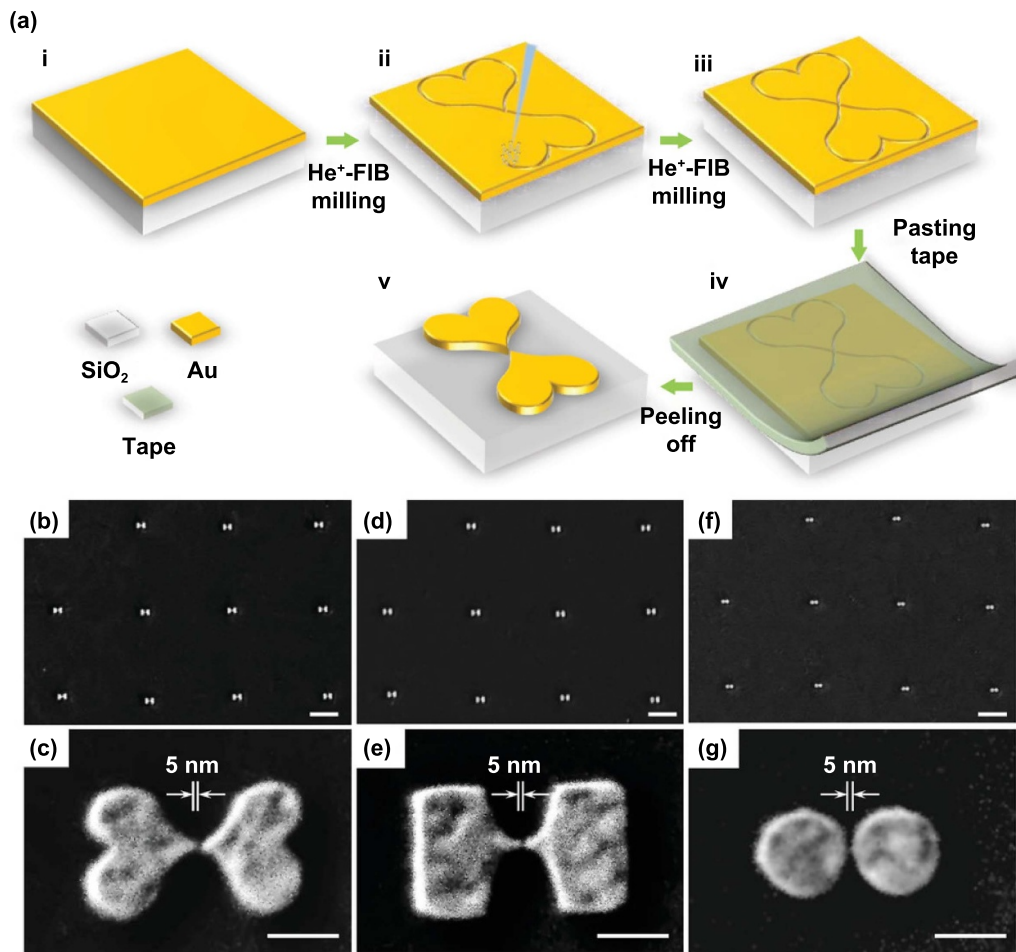


**Figure 16.** The fabrication methodology and the gallery of three kinds of Au nanoparticle dimers with different shapes. (a) The flowing charts of fabrication method to define heart-shaped nanoparticle dimer by  $\text{He}^+$ -FIB milling using the ‘sketch and peel’ strategy. (b), (d), (f) The SEM images of arrayed Au nanoparticle dimers with different shapes. (c), (e), (g) The corresponding high-resolution electron micrographs of single nanodimer. (b), (c) Heart-shaped; (d), (e) bowtie-shaped; (f), (g) disk-shaped nanoparticle dimer. Scale bars:  $1 \mu\text{m}$  in (b), (d), and (f);  $100 \text{ nm}$  in (c), (e), and (g). Reprinted with permission from [111]. Copyright 2020 John Wiley and Sons.

without the use of photo-masks, resist, or other expensive equipment.

## 6.2. Graphene devices

Due to its stability, high strength, resistance to defects, and unique electronic energy band structure, graphene material is widely used in nanoscale electronic, optoelectronic, and mechanical applications. HIB was used to controllably modify the electrical properties of graphene-based electronic devices by Marcus C M group with the direct writing technique [13]. As shown in figure 14(A), a channel about  $10 \text{ nm}$  wide was etched in a suspended graphene device to isolate different parts of the graphene field effect transistor. The electron transport performance of graphene nanoribbons was measured on an encapsulated graphene device with a  $10 \text{ nm}$  wide insulation barrier, which was etched by a  $30 \text{ keV}$  HIB [21]. As shown in figure 14(B), the HIB direct writing process was used to pattern graphene nanoribbon arrays as low as  $5 \text{ nm}$  wide for the first time. HIB direct writing technique was also used to create band gaps in graphene field effect transistors for electronic

sensing applications [22]. Naitou Y *et al* also patterned sub- $10 \text{ nm}$  wide nanoribbons on suspended monolayer graphene by HIB direct writing [99]. Scanning capacitance microscopy measurement results show that the spatial resolution of HIB pattern has a non-monotonic relationship with its dose. As shown in figure 14(C), the superstructures graphene nanoribbons with a pitch of  $20 \text{ nm}$  are directly written with a single-step pattern of defect lines with a width of  $5 \text{ nm}$  by HIB direct writing [100]. A set of graphene triangles were patterned using HIB direct writing technology for plasmon nanoresonator applications. The dose of helium ions greatly effects the plasmon response of graphene structures [101]. Although a lower dose of helium ions was bombarded on the graphene device, the residual conductivity attributed to hydrocarbon contamination should still be considered. Therefore, by using an improved HIM equipped with a commercial beam pattern package, Bell D C *et al* precisely cut and nanoscale patterned graphene by controlling the alignment, patterning, and exposure processes with a computer [102]. HIB allows for dosage control, pattern configurability, and precise alignment of existing features, all of which make HIB direct writing as fast

**Table 1.** The extreme nanofabrication with HIB technology.

Nanofabrication	Materials	Sizes of structure	Beam current (pA)	Beam dose or dwell time
HIB milling	Silicon nitride	Sub-5 nm nanopore [14]	1	0.3 s
	CNM	1.3 nm nanopore [12]	1.4	$4.5 \times 10^5$ ions
	Graphene	1.5 nm nanopore [59]	–	$8 \times 10^6$ ions nm <sup>-2</sup>
	h-BN	4 nm nanopore [57]	–	–
	MoS <sub>2</sub>	5 nm nanopore [59]	–	$8 \times 10^6$ ions nm <sup>-2</sup>
	Pt	15 nm width and 2 μm height pillar [78]	1	$1 \times 10^{15}$ ions cm <sup>-2</sup>
HIB-induced deposition	W	32 nm width and 7 μm height hollow nanowire [86]	1.15	379 μC
	Co	10 nm width line [83]	0.8	0.5 μs
	HSQ resist	4 nm half-pitch 8 nm lines [92]	1	90 pC cm <sup>-1</sup>
Additional HIB nanofabrication	Fullerene molecular resist	12 nm pitch and 6 nm width lines [93]	0.5	0.04 nC cm <sup>-1</sup>
	Alumina resist	5 nm isolated lines or 20 nm half-pitch 10 nm lines [94]	–	200–700 μC cm <sup>-2</sup>
	MOC resist	18 nm pitch and 5 nm width lines [95]	0.5	10 pC/cm <sup>-1</sup>
	Ni-MOCs resist	95 nm width lines [96]	0.55	8 pC cm <sup>-1</sup>
	Graphene	20 nm pitch and 5 nm width lines [100]	0.4	80 pC cm <sup>-1</sup>
	Au	5 nm gap [111]	–	–

lithography compatible technology for fabricating graphene devices [103].

### 6.3. Plasmonic nanostructures

Plasmonic nanostructures like metallic nano-antennas are widely used functional elements, such as molecular spectroscopy, near-field nanoscale imaging, and quantum mechanical phenomena. Coaxial optical antennae structures with a critical dimension less than 10 nm were directly fabricated using HIB direct writing technology for nano-optical applications. Due to the high-resolution fabrication capabilities of HIB, for the same design geometry, the quality factor of the fabricated coaxial antennae is higher than that of gallium FIB direct written resonators, as shown in figure 15(A) [104]. Figure 15(B) shows a 6 nm gap on the gold bowtie antennas, which were milled by HIB direct writing to investigate the quantum optical properties in a near-field plasmon nanoantenna with the third harmonic spectroscopy [23, 105]. Combined with electron lithography, HIB direct writing can fabricate the smallest size parts at low milling rates. Then, plasmonic nanoantennas could be patterned with the maximum precision in a reasonable time on the polycrystalline gold film or single-crystalline gold flakes [106]. As shown in figure 15(C), these strategies are used to further miniaturize zero-, first-, and second-order Sierpiński fractal dimer nanoantennas and to investigate the scattering spectrum and high near-field enhancement [107]. Plasmonic dipole nanoantennas with 5 nm-wide gaps were also fabricated by focused HIB direct writing. These antennas could have a wavelength shift

of about 250 nm per refractive index unit [24]. Moreover, a high-quality metal plasma heptamer nanohole array with an aspect ratio of 4:1 was fabricated by focused HIB direct writing [108]. For the plasmonic nanoantenna fabrication [109], HIB is a state-of-the-art nanofabrication technology, but its subtractive patterning strategy in nature and extremely low patterning efficiency make it unsuitable for plasmonic applications based on particle and assemblies. Therefore, Chen Y *et al* developed a sketch and peel strategy [110] enabling HIB to be utilized in the fabrication of plasmonic nanodimer with sub-10 nm nanogaps, as shown in figure 16. The two heart-shaped plasmonic nanodimers had both convex and concave features [111], which were obtained by topology optimization-based inverse designing. The heart-shaped nanodimers exhibited significantly stronger near-field enhancement performance than the bowtie-, and disk-shaped nanodimers structures in its sub-10 nm gap.

## 7. Outlook

The latest developments in HIB technology have been summarized, as shown in table 1. Generally, due to its high sensitivity and high resolution, HIB technology has been rapidly developed to fabricate more complicated nanostructures that can be used in a variety of applications. HIB technology is used for high-contrast, high-resolution imaging of conducting, semiconducting, and insulating materials, and biological samples. Although the ions collide with the target sample, HIB is superior to conventional SEM imaging. For extreme

nanofabrication, nanometer-scale nanopores that are beneficial for single base recognition of DNA/RNA sequences can be fabricated by HIB milling on thinned silicon nitride membranes or suspended graphene. Amorphization during the milling process promotes the formation of specific 3D nanopores, which can be used for potential nano-optics and bioscience applications. The chemical reaction of the precursor gas molecules adsorbed on the surface induced by HIB results in the direct deposition of programmed 3D structures at the nanoscale. HIB direct writing without resist assistance is used to pattern sub-10 nm nanochannels, nanoribbons, and nanostructures for nanoscale functional devices. Both HIM imaging and HIB nanofabrication must take into account the inevitable damage caused by helium ions colliding with the probe substrate. We can conclude that HIB technology is an attractive method for extreme nanofabrication because of its comprehensive advantages in sensitivity, resolution, and precision. For example, this technology takes advantage of the unique physical properties of graphene to facilitate graphene-based nanoelectronic devices used in a variety of applications, such as plasmon devices, one-step fabrication of solid-state nanopores in ultrathin membranes, etc.

HIB technology has a lower sputtering yield but can produce larger damage on the substrate in nanofabrication processing, such as bubbles, implantation, and amorphization. More in-depth theoretical research on the interaction mechanism between helium ions and materials has promoted the improvement of the processing capability of extreme nanofabrication with HIB technology. The stability and repeatability of the HIB milling process will be enhanced to meet the requirements of sub-nanometer resolution and high-throughput fabrication in special applications. Besides, when optimizing the nanofabrication process, the positive or negative impact of helium ions bombardment on the material properties should be considered, so that HIB technology can be used to directly fabricate nanostructures with fewer defects and excellent performance. For direct-write HIB technique and HIB-induced deposition processes, the common challenge is to increase the complexity of nanostructures while maintaining the nanoscale feature size for special applications. To increase the complexity of nanostructures and their applications in production, HIB direct writing must be improved through careful optimization of parameters. Furthermore, the proximity effect should also be taken into consideration in the HIB direct writing and HIB-induced deposition processes. In the end, HIB technology is expected to play an integral role in extreme nanofabrication because it has the advantages of high sensitivity, resolution, and precision for direct writing milling, patterning, assisted-milling and deposition processes with fewer damages to the samples.

## Acknowledgments

This work was supported by research funding from Natural Science Foundation of Chongqing, China (Grant No. cstc2018jcyjAX0310, cstc2017jcyjB0105, cstc2018jcyjAX0304), National Natural Science Foundation

of China (Grant Nos. 61701474, 31800711), Instrument development program of CAS(YZ201568), Pioneer Hundred Talents Program of CAS (Liang Wang) and Youth Innovation Promotion Association of the Chinese Academy of Sciences (2017392). The authors acknowledge Professor Duan Huigao for his invitation and the other peoples or presses for permitting to use their figures. We especially thank our colleagues from CIGIT for their information and encouragement in preparing this manuscript.

## ORCID iD

Deqiang Wang  <https://orcid.org/0000-0002-3151-6769>

## References

- [1] Scipioni L, Stern L A, Notte J, Sijbrandij S and Griffin B 2008 Helium ion microscope *Adv. Mater. Processes* **166** 27–30
- [2] Cohen-Tanugi D and Yao N 2008 Superior imaging resolution in scanning helium-ion microscopy: a look at beam-sample interactions *J. Appl. Phys.* **104** 063504
- [3] Zahid O K and Hall A R 2016 Helium ion microscope fabrication of solid-state nanopore devices for biomolecule analysis *Helium Ion Microscopy*, ed G Hlawacek and A Götzhäuser (Berlin: Springer) pp 447–70
- [4] Hill R, Notte J A and Scipioni L 2012 Scanning helium ion microscopy *Adv. Imaging Electron Phys.* **170** 65–148
- [5] Tan S D and Livengood R 2016 Applications of GFIS in semiconductors *Helium Ion Microscopy*, ed G Hlawacek and A Götzhäuser (Berlin: Springer) pp 471–98
- [6] Scipioni L, Alkemade P, Sidorkin V, Chen P, Maas D and van Veldhoven E 2009 The helium ion microscope: advances in technology and applications *Am. Lab.* **41** 26–8
- [7] Boden S A, Asadollahbaik A, Rutt H N and Bagnall D M 2012 Helium ion microscopy of Lepidoptera scales *Scanning* **34** 107–20
- [8] Alkemade P F A and van Veldhoven E 2012 Deposition, milling, and etching with a focused helium ion beam *Nanofabrication* eds M Stepanova and S Dew (Berlin: Springer) pp 275–300
- [9] Shorubalko I, Pillatsch L and Utke I 2016 Direct-write milling and deposition with noble gases *Helium Ion Microscopy*, ed G Hlawacek and A Götzhäuser (Berlin: Springer) pp 355–93
- [10] Yang J J, Ferranti D C, Stern L A, Sanford C A, Huang J, Ren Z, Qin L C and Hall A R 2011 Rapid and precise scanning helium ion microscope milling of solid-state nanopores for biomolecule detection *Nanotechnology* **22** 285310
- [11] Sawafta F, Clancy B, Carlsen A T, Huber M and Hall A R 2014 Solid-state nanopores and nanopore arrays optimized for optical detection *Nanoscale* **6** 6991–6
- [12] Emmrich D, Beyer A, Nadzeyka A, Bauerdick S, Meyer J C, Kotakoski J and Götzhäuser A 2016 Nanopore fabrication and characterization by helium ion microscopy *Appl. Phys. Lett.* **108** 163103
- [13] Lemme M C, Bell D C, Williams J R, Stern L A, Baugher B W H, Jarillo-Herrero P and Marcus C M 2009 Etching of graphene devices with a helium ion beam *ACS Nano* **3** 2674–6
- [14] Xia D Y, Huynh C, McVey S, Kobler A, Stern L, Yuan Z S and Ling X S 2018 Rapid fabrication of solid-state

- nanopores with high reproducibility over a large area using a helium ion microscope *Nanoscale* **10** 5198–204
- [15] Deng Y S, Huang Q M, Zhao Y, Zhou D M, Ying C F and Wang D Q 2016 Precise fabrication of a 5 nm graphene nanopore with a helium ion microscope for biomolecule detection *Nanotechnology* **28** 045302
- [16] Wang H T, Xie W Y, Wang Y J, Zhu J F, Liu M W, Lu W Q, Deng Y S, Wang G D and Wang D Q 2018 Fabrication of 3D nanovolcano-shaped nanopores with helium ion microscopy *J. Vac. Sci. Technol. B* **36** 011603
- [17] Alkemade P F A and Miro H 2014 Focused helium-ion-beam-induced deposition *Appl. Phys. A* **117** 1727–47
- [18] Utke I, Hoffmann P and Melngailis J 2008 Gas-assisted focused electron beam and ion beam processing and fabrication *J. Vac. Sci. Technol. B* **26** 1197–276
- [19] Drezner Y, Greenzweig Y, Fishman D, van Veldhoven E, Maas D J, Raveh A and Livengood R H 2012 Structural characterization of He ion microscope platinum deposition and sub-surface silicon damage *J. Vac. Sci. Technol. B* **30** 041210
- [20] Shi X Q and Boden S A 2016 Scanning helium ion beam lithography *Front. Nanosci.* **11** 563–94
- [21] Nanda G, Hlawacek G, Goswami S, Watanabe K and Taniguchi T 2017 Alkemade P F A. Electronic transport in helium-ion-beam etched encapsulated graphene nanoribbons *Carbon* **119** 419–25
- [22] Abbas A N, Liu G, Liu B L, Zhang L Y, Liu H, Ohlberg D, Wu W and Zhou C W 2014 Patterning, characterization, and chemical sensing applications of graphene nanoribbon arrays down to 5 nm using helium ion beam lithography *ACS Nano* **8** 1538–46
- [23] Kollmann H *et al* 2014 Toward plasmonics with nanometer precision: nonlinear optics of helium-ion milled gold nanoantennas *Nano Lett.* **14** 4778–84
- [24] Scholder O, Jefimovs K, Shorubalko I, Hafner C, Sennhauser U and Bona G L 2013 Helium focused ion beam fabricated plasmonic antennas with sub-5 nm gaps *Nanotechnology* **24** 395301
- [25] Reimer L 2000 Scanning electron microscopy: physics of image formation and microanalysis, second edition *Meas. Sci. Technol.* **11** 1826
- [26] Arey B W, Shutthanandan V and Jiang W 2010 *Helium Ion Microscopy Versus Scanning Electron Microscopy* (New York: Wiley)
- [27] Bell D C 2009 Contrast mechanisms and image formation in helium ion microscopy *Microsc. Microanal.* **15** 147–53
- [28] Hlawacek G, Veligura V, van Gastel R and Poelsema B 2014 Helium ion microscopy *J. Vac. Sci. Technol. B* **32** 020801
- [29] Scipioni L, Sanford C A, Notte J, Thompson B and McVey S 2009 Understanding imaging modes in the helium ion microscope *J. Vac. Sci. Technol. B* **27** 3250–5
- [30] Wirtz T, De Castro O, Audinot J N and Philipp P 2019 Imaging and analytics on the helium ion microscope *Annu. Rev. Anal. Chem.* **12** 523–43
- [31] Ward B W, Notte J A and Economou N P 2006 Helium ion microscope: a new tool for nanoscale microscopy and metrology *J. Vac. Sci. Technol. B* **24** 2871–4
- [32] Götzhäuser A and Hlawacek G 2016 HIM of biological samples *Helium Ion Microscopy*, ed G Hlawacek and A Götzhäuser (Berlin: Springer) pp 173–85
- [33] Bazou D, Behan G, Reid C, Boland J J and Zhang H Z 2011 Imaging of human colon cancer cells using He-Ion scanning microscopy *J. Microsc.* **242** 290–4
- [34] Vanden Berg-Foels W S, Scipioni L, Huynh C and Wen X 2012 Helium ion microscopy for high-resolution visualization of the articular cartilage collagen network *J. Microsc.* **246** 168–76
- [35] Joens M S *et al* 2013 Helium Ion Microscopy (HIM) for the imaging of biological samples at sub-nanometer resolution *Sci. Rep.* **3** 3514
- [36] Boseman A, Nowlin K, Ashraf S, Yang J J and LaJeunesse D 2013 Ultrastructural analysis of wild type and mutant *Drosophila melanogaster* using helium ion microscopy *Micron* **51** 26–35
- [37] Rice W L, van Hoek A N, Păunescu T G, Huynh C, Goetze B, Singh B, Scipioni L, Stern L A and Brown D 2013 High resolution helium ion scanning microscopy of the rat kidney *PloS One* **8** e57051
- [38] Leppänen M, Sundberg L R, Laanto E, de Freitas Almeida G M, Papponen P and Maasilta I J 2017 Imaging bacterial colonies and phage–bacterium interaction at sub-nanometer resolution using helium-ion microscopy *Adv. Biosyst.* **1** 1700070
- [39] Dykas M M, Poddar K, Yoong S L, Viswanathan V, Mathew S, Patra A, Saha S, Pastorin G and Venkatesan T 2018 Enhancing image contrast of carbon nanotubes on cellular background using helium ion microscope by varying helium ion fluence *J. Microsc.* **269** 14–22
- [40] Iberi V, Vlasiouk I, Zhang X G, Matola B, Linn A, Joy D C and Rondinone A J 2015 Maskless lithography and *in situ* visualization of conductivity of graphene using helium ion microscopy *Sci. Rep.* **5** 11952
- [41] Sakai C, Ishida N, Masuda H, Nagano S, Kitahara M, Ogata Y and Fujita D 2016 Active voltage contrast imaging of cross-sectional surface of multilayer ceramic capacitor using helium ion microscopy *Appl. Phys. Lett.* **109** 051603
- [42] Sakai C, Ishida N, Nagano S, Onishi K and Fujita D 2018 *In situ* voltage-application system for active voltage contrast imaging in helium ion microscope *J. Vac. Sci. Technol. B* **36** 042903
- [43] Xia D Y, McVey S, Huynh C and Kuehn W 2019 Defect localization and nanofabrication for conductive structures with voltage contrast in helium ion microscopy *ACS Appl. Mater. Interfaces* **11** 5509–16
- [44] Xia D Y, McVey S and Kuehn W 2019 Defect localization and electrical fault isolation for metal connection using helium ion microscope *Proc. 2019 Int. Symp. on VLSI Technology, Systems and Application (IEEE, Hsinchu, China)* pp 1–2
- [45] Hlawacek G, Jankowski M, Wormeester H, van Gastel R, Zandvliet H J W and Poelsema B 2016 Visualization of steps and surface reconstructions in Helium Ion Microscopy with atomic precision *Ultramicroscopy* **162** 17–24
- [46] Jepson M A E, Inkson B J, Liu X, Scipioni L and Rodenburg C 2009 Quantitative dopant contrast in the helium ion microscope *EPL* **86** 26005
- [47] Jepson M A E, Inkson B J, Rodenburg C and Bell D C 2009 Dopant contrast in the helium ion microscope *EPL* **85** 46001
- [48] Hlawacek G, Veligura V, Lorbek S, Mocking T F, George A, van Gastel R, Zandvliet H J W and Poelsema B 2012 Imaging ultra thin layers with helium ion microscopy: utilizing the channeling contrast mechanism *Beilstein J. Nanotechnol.* **3** 507–12
- [49] Hall A R 2013 In situ thickness assessment during ion milling of a free-standing membrane using transmission helium ion microscopy *Microsc. Microanal.* **19** 740–4
- [50] Guo H X, Itoh H, Wang C M, Zhang H and Fujita D 2014 Focal depth measurement of scanning helium ion microscope *Appl. Phys. Lett.* **105** 023105
- [51] Huang Z, W D L, Santori C, Acosta V M, Faraon A, Ishikawa T, Wu W, Winston D, Williams R S and Beausoleil R G 2013 Diamond nitrogen-vacancy centers

- created by scanning focused helium ion beam and annealing *Appl. Phys. Lett.* **103** 081906
- [52] Livengood R, Tan S D, Greenzweig Y, Notte J and McVey S 2009 Subsurface damage from helium ions as a function of dose, beam energy, and dose rate *J. Vac. Sci. Technol. B* **27** 3244–9
- [53] Wasfi A, Awwad F and Ayesh A I 2018 Graphene-based nanopore approaches for DNA sequencing: a literature review *Biosens. Bioelectron.* **119** 191–203
- [54] Marshall M M, Yang J J and Hall A R 2012 Direct and transmission milling of suspended silicon nitride membranes with a focused helium ion beam *Scanning* **34** 101–6
- [55] Carlsen A T, Briggs K, Hall A R and Tabard-Cossa V 2017 Solid-state nanopore localization by controlled breakdown of selectively thinned membranes *Nanotechnology* **28** 085304
- [56] Sawafta F, Carlsen A T and Hall A R 2014 Membrane thickness dependence of nanopore formation with a focused helium ion beam *Sensors* **14** 8150–61
- [57] Chen D X *et al* 2019 Sub-10 nm stable graphene quantum dots embedded in hexagonal boron nitride *Nanoscale* **11** 4226–30
- [58] Knust S, Kreft D, Hillmann R, Meyer A, Viefhues M, Reimann P and Anselmetti D 2017 Measuring DNA translocation forces through MoS<sub>2</sub>-nanopores with optical tweezers *Mater. Today Proc.* **4** S168–S173
- [59] Hayashi T, Arima K, Yamashita N, Park S, Ma Z P, Tabata O and Kawai K 2018 Nanopore fabrication of two-dimensional materials on SiO<sub>2</sub> membranes using helium ion microscopy *IEEE Trans. Nanotechnol.* **17** 727–30
- [60] Fox D, Zhou Y B, O'Neill A, Kumar S, Wang J J, Coleman J N, Duesberg G S, Donegan J F and Zhang H Z 2013 Helium ion microscopy of graphene: beam damage, image quality and edge contrast *Nanotechnology* **24** 335702
- [61] Buchheim J, Wyss R M, Shorubalko I and Park H G 2016 Understanding the interaction between energetic ions and freestanding graphene towards practical 2D perforation *Nanoscale* **8** 8345–54
- [62] Cantley L *et al* 2019 Voltage gated inter-cation selective ion channels from graphene nanopores *Nanoscale* **11** 9856–61
- [63] Schmidt M E, Iwasaki T, Muruganathan M, Haque M, van Ngoc H, Ogawa S and Mizuta H 2018 Structurally controlled large-area 10 nm pitch graphene nanomesh by focused helium ion beam milling *ACS Appl. Mater. Interfaces* **10** 10362–8
- [64] Zhang L, Heinig N F, Bazargan S, Abd-Ellah M, Moghimi N and Leung K T 2015 Direct-write three-dimensional nanofabrication of nanopillars and nanocones on Si by nanotumefaction using a helium ion microscope *Nanotechnology* **26** 255303
- [65] Córdoba R, Ibarra A and Mailly D 2018 de Teresa J M. Vertical growth of superconducting crystalline hollow nanowires by He<sup>+</sup> focused ion beam induced deposition *Nano Lett.* **18** 1379–86
- [66] Lee C L, Chien S W, Chen S Y, Liu C H, Tsai K Y, Li J H, Shew B Y, Hong C S and Lee C T 2017 Fabrication of metrology test structures with helium ion beam direct write *Proc. SPIE 10145, Metrology, Inspection, and Process Control for Microlithography XXXI (SPIE, San Jose, CA, USA)* p 1014519
- [67] Lee C L, Cai J S, Chien S W and Tsai K Y 2019 Precision fabrication of EUVL programmed defects with helium ion beam lithography *Proc. SPIE 11147, Int. Conf. on Extreme Ultraviolet Lithography 2019 (SPIE, Monterey, CA, USA)* p 111471J
- [68] Scipioni L, Ferranti D C, Smentkowski V S and Potyralo R A 2010 Fabrication and initial characterization of ultrahigh aspect ratio vias in gold using the helium ion microscope *J. Vac. Sci. Technol. B* **28** C6P18–23
- [69] Giri P K, Raineri V, Franzo G and Rimini E 2001 Mechanism of swelling in low-energy ion-irradiated silicon *Phys. Rev. B* **65** 012110
- [70] Giri P K 2005 Studies on the surface swelling of ion-irradiated silicon: role of defects *Mater. Sci. Eng. B* **121** 238–43
- [71] Leclerc S, Declémy A, Beaufort M F, Tromas C and Barbot J F 2005 Swelling of SiC under helium implantation *J. Phys. D: Appl. Phys.* **98** 113506
- [72] Tseng A A 2005 Recent developments in nanofabrication using focused ion beams *Small* **1** 924–39
- [73] Mitsui T, Stein D, Kim Y R, Hoogerheide D and Golovchenko J A 2006 Nanoscale volcanoes: accretion of matter at ion-sculpted nanopores *Phys. Rev. Lett.* **96** 036102
- [74] Livengood R H, Greenzweig Y, Liang T and Grumski M 2007 Helium ion microscope invasiveness and imaging study for semiconductor applications *J. Vac. Sci. Technol. B* **25** 2547–52
- [75] Sanford C A, Stern L, Barriss L, Farkas L, DiManna M, Mello R, Maas D J and Alkemade P F 2009 Beam induced deposition of platinum using a helium ion microscope *J. Vac. Sci. Technol. B* **27** 2660–7
- [76] Alkemade P F A, Chen P, van Veldhoven E and Maas D 2010 Model for nanopillar growth by focused helium ion-beam-induced deposition *J. Vac. Sci. Technol. B* **28** C6F22–C6F25
- [77] Wu H M, Stern L A, Chen J H, Huth M, Schwalb C H, Winhold M, Porrati F, Gonzalez C M, Timilsina R and Rack P D 2013 Synthesis of nanowires via helium and neon focused ion beam induced deposition with the gas field ion microscope *Nanotechnology* **24** 175302
- [78] Alkemade P F A, Miro H, van Veldhoven E, Maas D J, Smith D A and Rack P D 2011 Pulsed helium ion beam induced deposition: a means to high growth rates *J. Vac. Sci. Technol. B* **29** 06FG05
- [79] Yang P S, Huang Z D, Huang K W and Chen M J 2020 Selective growth of platinum nanolines by helium ion beam induced deposition and atomic layer deposition *Ultramicroscopy* **211** 112952
- [80] Timilsina R, Smith D A and Rack P D 2013 A comparison of neon versus helium ion beam induced deposition via Monte Carlo simulations *Nanotechnology* **24** 115302
- [81] Smith D A, Joy D C and Rack P D 2010 Monte Carlo simulation of focused helium ion beam induced deposition *Nanotechnology* **21** 175302
- [82] Chen P, van Veldhoven E, Sanford C A, Salemink H W M, Maas D J, Smith D A, Rack P D and Alkemade P F A 2010 Nanopillar growth by focused helium ion-beam-induced deposition *Nanotechnology* **21** 455302
- [83] Kohama K, Iijima T, Hayashida M and Ogawa S 2013 Tungsten-based pillar deposition by helium ion microscope and beam-induced substrate damage *J. Vac. Sci. Technol. B* **31** 031802
- [84] Wu H, Stern L A, Xia D, Ferranti D, Thompson B, Klein K L, Gonzalez C M and Rack P D 2014 Focused helium ion beam deposited low resistivity cobalt metal lines with 10 nm resolution: implications for advanced circuit editing *J. Mater. Sci. Mater. Electron.* **25** 587–95
- [85] Boden S A, Moktadir Z, Bagnall D M, Mizuta H and Rutt H N 2011 Focused helium ion beam milling and deposition *Microelectron. Eng.* **88** 2452–5

- [86] Basset J *et al* 2019 High kinetic inductance microwave resonators made by He-Beam assisted deposition of tungsten nanowires *Appl. Phys. Lett.* **114** 102601
- [87] Córdoba R, Maily D, Rezaev R O, Smirnova E I, Schmidt O G, Fomin V M, Zeitler U, Guillaumon I, Suderow H and de Teresa J M 2019 Three-dimensional superconducting nanohelices grown by He<sup>+</sup>-focused-ion-beam direct writing *Nano Lett.* **19** 8597–604
- [88] Horák M, Bukvišová K, Švarc V, Jaskowiec J, Krápek V and Šíkola T 2018 Comparative study of plasmonic antennas fabricated by electron beam and focused ion beam lithography *Sci. Rep.* **8** 9640
- [89] Winston D *et al* 2009 Scanning-helium-ion-beam lithography with hydrogen silsesquioxane resist *J. Vac. Sci. Technol. B* **27** 2702–6
- [90] Ruchhoeft P and Wolfe J C 2000 Determination of resist exposure parameters in helium ion beam lithography: absorbed energy gradient, contrast, and critical dose *J. Vac. Sci. Technol. B* **18** 3177–80
- [91] Kalhor N and Alkemade P F A 2016 Resist assisted patterning *Helium Ion Microscopy*, ed G Hlawacek and A Götzhäuser (Berlin: Springer) pp 395–414
- [92] Li W D, Wu W and Williams R S 2012 Combined helium ion beam and nanoimprint lithography attains 4 nm half-pitch dense patterns *J. Vac. Sci. Technol. B* **30** 06F304
- [93] Shi X Q, Prewett P, Huq E, Bagnall D M, Robinson A P G and Boden S A 2016 Helium ion beam lithography on fullerene molecular resists for sub-10 nm patterning *Microelectron. Eng.* **155** 74–78
- [94] Cattoni A, Maily D, Dalstein O, Faustini M, Seniutinas G, Rösner B and David C 2018 Sub-10 nm electron and helium ion beam lithography using a recently developed alumina resist *Microelectron. Eng.* **193** 18–22
- [95] Lewis S M *et al* 2019 Plasma-etched pattern transfer of sub-10 nm structures using a metal–organic resist and helium ion beam lithography *Nano Lett.* **19** 6043–8
- [96] Kumar R, Chauhan M, Moinuddin M G, Sharma S K and Gonsalves K E 2020 Development of nickel-based negative tone metal oxide cluster resists for sub-10 nm electron beam and helium ion beam lithography *ACS Appl. Mater. Interfaces* **12** 19616–24
- [97] Flatabø R, Agarwal A, Hobbs R, Greve M M, Holst B and Berggren K K 2018 Exploring proximity effects and large depth of field in helium ion beam lithography: large-area dense patterns and tilted surface exposure *Nanotechnology* **29** 275301
- [98] Cai J X, Zhu Z Y, Alkemade P F A, van Veldhoven E, Wang Q J, Ge H X, Rodrigues S P, Cai W S and Li W D 2018 3D volumetric energy deposition of focused helium ion beam lithography: visualization, modeling, and applications in nanofabrication *Adv. Mater. Interfaces* **5** 1800203
- [99] Naitou Y, Iijima T and Ogawa S 2015 Direct nano-patterning of graphene with helium ion beams *Appl. Phys. Lett.* **106** 033103
- [100] Archanjo B S, Fragneaud B, Cançado L C, Winston D, Miao F, Achete C A and Medeiros-Ribeiro G 2014 Graphene nanoribbon superlattices fabricated via He ion lithography *Appl. Phys. Lett.* **104** 193114
- [101] Jiang X J, Cai W, Luo W W, Xiang Y X, Zhang N, Ren M X, Zhang X Z and Xu J J 2018 Near-field imaging of graphene triangles patterned by helium ion lithography *Nanotechnology* **29** 385205
- [102] Bell D C, Lemme M C, Stern L A, Williams J R and Marcus C M 2009 Precision cutting and patterning of graphene with helium ions *Nanotechnology* **20** 455301
- [103] Hang S, Moktadir Z, Kalhor N, Saito S and Mizuta H 2013 Direct helium ion milling technology: towards the fabrication of extremely down-scaled graphene nanodevices *Proc. 2013 IEEE Silicon Nanoelectronics Workshop* (IEEE, Kyoto, Japan)
- [104] Melli M, Polyakov A, Gargas D, Huynh C, Scipioni L, Bao W, Ogletree D F, Schuck P J, Cabrini S and Weber-Bargioni A 2013 Reaching the theoretical resonance quality factor limit in coaxial plasmonic nanoresonators fabricated by helium ion lithography *Nano Lett.* **13** 2687–91
- [105] Kollmann H *et al* Ultrafast third-harmonic spectroscopy of single nanoantennas fabricated using helium-ion beam lithography 2016 *Proc. SPIE 9759, Advanced Fabrication Technologies for Micro/Nano Optics and Photonics IX* (SPIE, San Francisco, CA, USA)
- [106] Laible F, Dreser C, Kern D P and Fleischer M 2019 Time-effective strategies for the fabrication of poly- and single-crystalline gold nano-structures by focused helium ion beam milling *Nanotechnology* **30** 235302
- [107] Seitz L, Laible F, Dickreuter S, Gollmer D A, Kern D P and Fleischer M 2019 Miniaturized fractal optical nanoantennas defined by focused helium ion beam milling *Nanotechnology* **31** 075301
- [108] Hahn C, Hajebifard A and Berini P 2020 Helium focused ion beam direct milling of plasmonic heptamer-arranged nanohole arrays *Nanophotonics* **9** 393–9
- [109] Wang Y D, Abb M, Boden S A, Aizpurua J, de Groot C H and Muskens O L 2013 Ultrafast nonlinear control of progressively loaded, single plasmonic nanoantennas fabricated using helium ion milling *Nano Lett.* **13** 5647–53
- [110] Chen Y Q, Bi K X, Wang Q J, Zheng M J, Liu Q, Han Y X, Yang J B, Chang S L, Zhang G H and Duan H G 2016 Rapid focused ion beam milling based fabrication of plasmonic nanoparticles and assemblies via ‘sketch and peel’ strategy *ACS Nano* **10** 11228–36
- [111] Chen Y Q, Hu Y Q, Zhao J Y, Deng Y S, Wang Z L, Cheng X, Lei D Y, Deng Y B and Duan H G 2020 Topology optimization-based inverse design of plasmonic nanodimer with maximum near-field enhancement *Adv. Funct. Mater.* **30** 2000642